

Technical Report

TR-22-14

March 2023



EBS TF – THM modelling

Water transport in pellets-filled slots
– evaluation of Subtask B and final evaluation

Mattias Åkesson

SVENSK KÄRNBRÄNSLEHANTERING AB

SWEDISH NUCLEAR FUEL
AND WASTE MANAGEMENT CO

Box 3091, SE-169 03 Solna
Phone +46 8 459 84 00
skb.se

SVENSK KÄRNBRÄNSLEHANTERING

ISSN 1404-0344

SKB TR-22-14

ID 1996275

March 2023

EBS TF – THM modelling

Water transport in pellets-filled slots – evaluation of Subtask B and final evaluation

Mattias Åkesson, Svensk Kärnbränslehantering AB

This report is published on www.skb.se

© 2023 Svensk Kärnbränslehantering AB

Abstract

A modelling task, denoted “Water transport in pellets-filled slots” has been performed within the EBS Taskforce. The aim of this task was to investigate the ability of models (existing or new) to simulate water transport at different test conditions. Two subtasks which addressed two test types: A) 1D-tests with water freely available (water uptake tests), and C) 1D-tests with water redistribution in a temperature gradient, have previously been reported and evaluated (see Åkesson 2020).

This report includes an evaluation of a subtask B which addressed a test type with constant water inflow rate from a point inflow. The following modelling teams have contributed to the task and have been using different numerical codes: i) the Posiva team, from Elomatic Oy, using StarCCM+; ii) the NWS team, from Jacobs Clean Energy Limited, using COMSOL Multiphysics; iii) the SKB team, using COMSOL Multiphysics; and iv) the SKB1 team, from Clay Technology AB, also using COMSOL Multiphysics. All contributions have included some description of the water transport in the pore systems between the pellets (i.e. macro flow). Three of the teams used Darcy’s law and some form of water retention curve; two of them used an unusual retention curve with which the liquid pressure exceeded the gas pressure. In contrast, one team used two-phase flow description in which no water retention curve was employed. All teams included some form of water absorption, which in turn reduced the permeability and thereby sealed the macro flow. Two teams had a representation of water transport in the absorbed water (i.e. micro voids). Three of the teams included a representation of piping and channel formation.

The report also presents an outlook for further model developments, in which the role of different processes involved in the water saturation is discussed. The following three topics are addressed: i) dismantling data from the Prototype repository; ii) a tentative description of the water saturation processes, and iii) a discussion of the hydromechanical interaction between the buffer/backfill-system and the near-field rock.

Sammanfattning

En beräkningsuppgift, benämnd "Vattentransport i pelletsfyllda spalter" har utförts inom samarbetsprojektet "Taskforce on Engineered Barrier Systems". Målet med denna var att undersöka olika materialmodellens förmåga att simulera vattentransport under olika testförhållanden. Två deluppgifter har tidigare rapporterats och utvärderats (se Åkesson 2020). Dessa inriktades mot två testtyper: A) 1D-tester med fri tillgång på vatten (vattenuptagsförsök), och C) 1D-tester med fuktomfördelning i en temperaturgradient.

Denna rapport innehåller en utvärdering av deluppgift B, vilken inriktades mot en testtyp med konstant inflödes hastighet från en inflödespunkt. Följande modelleringsgrupper har bidragit till uppgiften och har använt olika numeriska koder: POSIVA-teamet, från Elomatic Oy med StarCCM+; ii) NWS-teamet från Jacobs Clean Energy Limited, med COMSOL Multi-physics; iii) SKB-teamet med COMSOL Multiphysics; och iv) SKB1-teamet, från Clay Technology AB som också har använt COMSOL Multiphysics. Samtliga bidrag har inkluderat en beskrivning av vattentransport i porsystemet mellan pellets (s k makroflöde). Tre av grupperna använde Darcy's lag och någon slags vattenretentionskurva; två av dessa använde en ovanlig retentionskurva med vilken vätsketrycket översteg gastrycket. Till skillnad från dessa använde ett team en tvåfas-flödesbeskrivning med vilken det inte ingick någon vattenretentionskurva. Samtliga grupper inkluderade någon form av vattenabsorption, vilket i sin tur medförde en reducerad permeabilitet och därmed tätade till makroflödet. I två av bidragen ingick en representation av vattentransport i det absorberade vattnet (i så kallade mikroporer). Tre av grupperna inkluderade en representation av kanalbildning.

I rapporten presenteras också en framåtblickande diskussion om ytterligare modellutveckling, vilken behandlar de olika processerna som ingår vid vattenuptag. Följande tre ämnen tas upp: i) brytningsdata från Prototypförvaret; ii) en övergripande beskrivning av vattenmättnadsprocessen, och iii) en diskussion kring den hydromekaniska interaktionen mellan buffert och återfyllning å ena sidan, och omgivande närzonsberg å andra sidan.

Contents

| | | |
|-----------------|---|----|
| 1 | Introduction | 7 |
| 2 | Re-cap of subtask A and C | 9 |
| 3 | Subtask B | 11 |
| 3.1 | Test setup | 11 |
| 3.2 | Wetting pattern | 14 |
| 3.3 | Task description | 14 |
| 4 | Model contributions | 15 |
| 4.1 | Posiva/Elomatic | 15 |
| 4.2 | NWS/Jacobs | 17 |
| 4.3 | SKB | 19 |
| 4.4 | SKB1/Claytech | 21 |
| 4.5 | Comparison of material models | 23 |
| 5 | Evaluation | 25 |
| 5.1 | Macro retention | 25 |
| 5.2 | Saturation fronts | 26 |
| 5.3 | Permeability relations | 28 |
| 5.4 | Absorption rates | 28 |
| 5.5 | Channel pressure | 30 |
| 5.6 | Channel formation | 31 |
| 5.7 | Comments | 31 |
| 6 | Outlook for further developments | 33 |
| 6.1 | Introduction | 33 |
| 6.2 | Field experiment data | 33 |
| 6.3 | Flow systems and phases | 35 |
| 6.4 | Hydromechanical interactions | 36 |
| 7 | Concluding remarks | 39 |
| | References | 41 |
| Appendix | Task description | 43 |

1 Introduction

A modelling task denoted “Water transport in pellets-filled slots” was defined within the framework of EBS Taskforce during 2016. The aim of this was to formulate new models or use existing models for water transport in pellet fillings and to calibrate and check their ability to model water transport at different boundary and inflow conditions and at different temperature situations.

Four different subtasks were originally proposed:

- Subtask A. 1D-tests with water freely available (water uptake tests).
- Subtask B. Constant water inflow rate from point inflow.
- Subtask C. 1D-tests with water redistribution in a temperature gradient.
- Subtask D. 1D-tests with water freely available in a temperature gradient.

These subtasks were planned to be based on experimental data from four corresponding test types. However, due to limited resources, only tests within two of the subtasks (A and C) could initially be performed, and a first task description was distributed in September 2016. These subtasks were finalized in 2019, and an evaluation of the different contributions to the subtasks was presented by Åkesson (2020). A task description for subtask B was distributed in June 2018 (see Appendix). This was based on experimental work performed by Saanio & Riekkola Oy and financed by Posiva Oy. This subtask was finalized in 2022.

The objective of this report is first and foremost to present a summary and an evaluation of the different modelling work that has been performed within the framework of Subtask B. The following modelling teams, using different numerical codes, have contributed and submitted reports:

- POSIVA team, from Elomatic Oy, using StarCCM+.
- NWS team, from Jacobs Clean Energy Limited, using COMSOL Multiphysics.
- SKB team, using COMSOL Multiphysics.
- SKB1 team, from Clay Technology AB, using COMSOL Multiphysics.

Secondly, this report also includes a discussion of the role of different processes involved in the water saturation of buffer and backfill materials, and addresses the following three topics: i) dismantling data from the Prototype repository; ii) a tentative description of the water saturation processes as being composed of three flow systems and four phases, and iii) a discussion of the hydromechanical interaction between the buffer/backfill-system and the near-field rock.

A re-cap of subtask A & C and the main findings from these are presented in Chapter 2. A description of subtask B and some of the experimental data on which this subtask is based are presented in Chapter 3. A summary of the model contributions and their material models and modelling approaches is presented in Chapter 4. Comparisons and evaluations of the different contributions are presented in Chapter 5. An outlook for further model developments, in which the role of different processes involved in the water saturation is discussed, is presented in Chapter 6. Finally, some concluding remarks are given in Chapter 7.

2 Re-cap of subtask A and C

Subtasks A and C addressed water transport in simple and well-defined test conditions. Both cases were based on tests which were performed in cylindrical tubes (with diameter 0.1 m and length 0.5 m): in subtask A with isothermal conditions (room temperature) and with free access of water at one of the ends; in subtask C with no water addition and with a temperature difference along the length of the cylinder (from 24 to 74 °C). Both test geometries were thus essentially one dimensional, although some minor thermal losses on the lateral sides could not be avoided in subtask C. The relative humidity was monitored at different points in both test types, and the water content distribution along the cylinder was measured at the end of each test. The main task in both of the subtasks were therefore to simulate the RH-evolution and the final water content distribution in the analysed tests.

Four modelling teams using different codes contributed and submitted results: i) SKB, ii) RWM with a team from Wood Nuclear Limited, iii) SKB1 with a team from Clay Technology AB, and iv) Posiva with a team from Universidad de Castilla-La Mancha (UCLM). The used material models included established constitutive relations: i) water retention curves; ii) the Darcy's law for unsaturated liquid transport; and iii) vapor diffusion, and the presented modelling work showed that these constitutive relations essentially can describe the processes in both the investigated test types.

The reason for this seems to be that the test conditions defined by the liquid pressure boundary (subtask A) or by a temperature profile (subtask C) meant that the processes were slow enough to sustain a thermodynamic equilibrium between water activity in macro pores and in the interlayer clay water (Figure 2-1 upper panels). Macro-pores are therefore essentially gas-filled which means that the water transport is governed by the same interlayer HM mechanisms which determine the hydraulic conductivity at saturated conditions.

In contrast, the established TH models are not sufficiently suited for conditions in which the inflow rate is governed by an external process, as in test type B. A typical example of such a situation is the localized water inflow into a pellets-filled slot through a fracture intersecting a deposition hole. This will imply the non-equilibrium between macro pores and the interlayer, which in turn can lead to water transport through the macro-pores (Figure 2-1 lower panel).

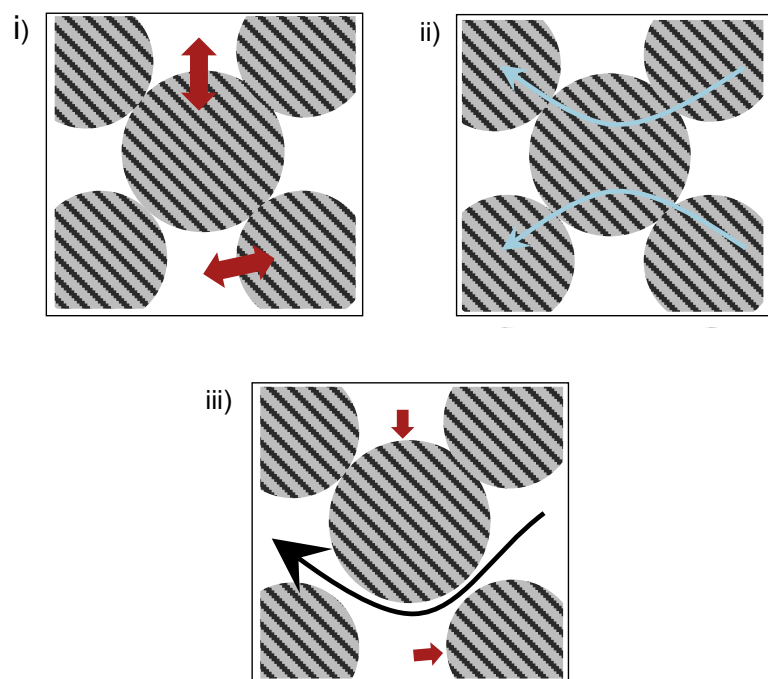


Figure 2-1. Schematic illustration of water-filled micro-pores in pellets and macro-pores. Condition with equilibrium between pore systems (i), water transport through micro-pores (ii), and condition without equilibrium and with water transport through macro-pores (iii).

The presented models also showed that vapor transport governed by diffusion is a quite accurate and sufficient description of the processes in the investigated test types. However, this result may be due the situation in which the temperature gradient is parallel to the direction of gravity. If these vectors would be perpendicular, which is largely the case in the pellets-filled slot in a deposition hole, then it can be expected that the influence of natural convection would be more significant (Figure 2-2).

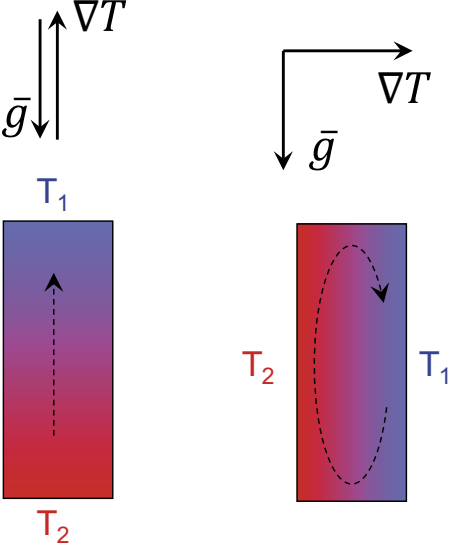


Figure 2-2. Schematic illustration of expected influence of gravity on vapor transport, parallel and perpendicular to thermal gradient.

3 Subtask B

This chapter presents a short overview of the laboratory tests, the test results, the used pellets materials and the requested model results. A more detailed description of these tests is given by Martikainen et al. (2017) and in the task description given in full in Appendix.

3.1 Test setup

Two test types were used: i) bucket tests, performed in a 200 litre bucket (Figure 3-1); and ii) box tests, performed in a 571 litre box, which were either unloaded (Figure 3-2) or loaded at the top (Figure 3-3). In both test types, the target for the water inflow rate was 0.005 l/min.

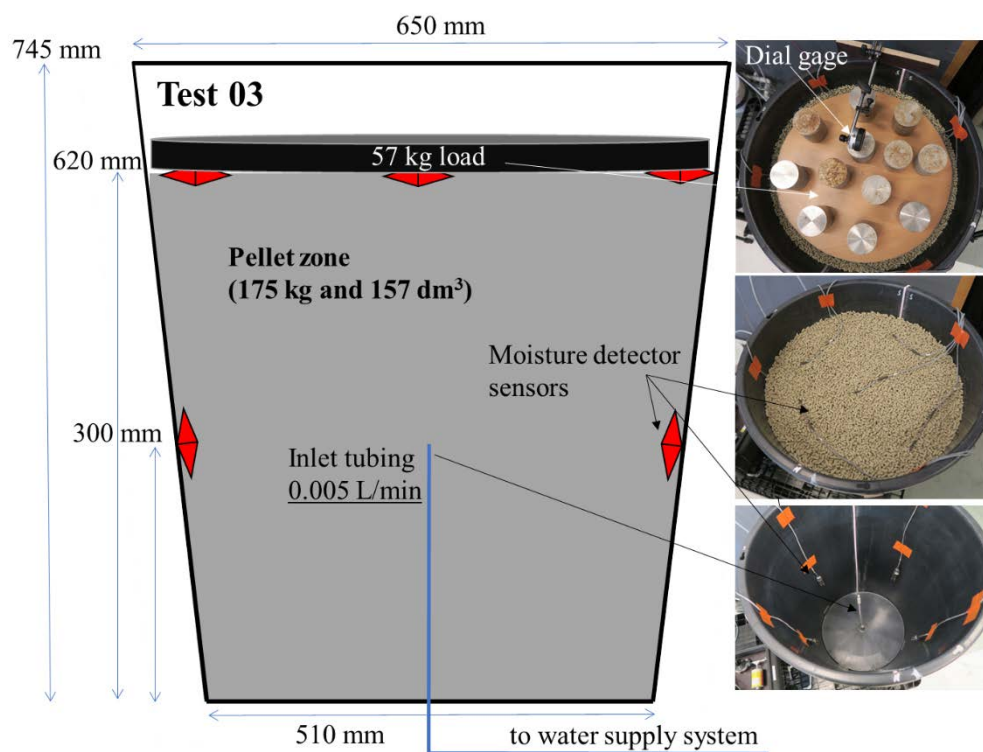


Figure 3-1. Cross-section schematic illustration of the test system (left) with initial pellet volume dimensions, water inlet position and location of moisture detector sensors and photographic images (right) showing test setup in the 3D wetting test 03. A surface load (57 kg) on the top of the pellet-filling was used in test 03. A dial gage measured vertical displacement at the top of the surface load. The inlet tubing was led through the bottom at the centre of the bucket.

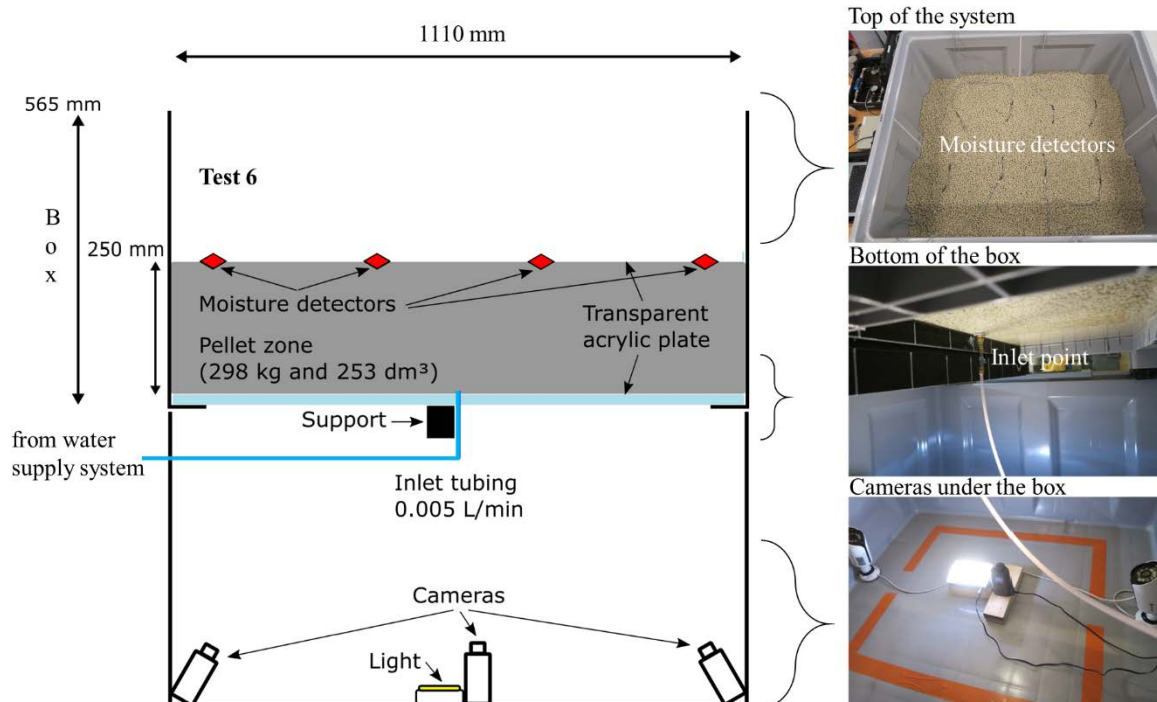


Figure 3-2. Cross-section schematic illustration of the test system (left) showing test setup, initial pellet volume dimensions, water inlet position and location of moisture detector sensors and photographic images (right) of floor wetting test 06.

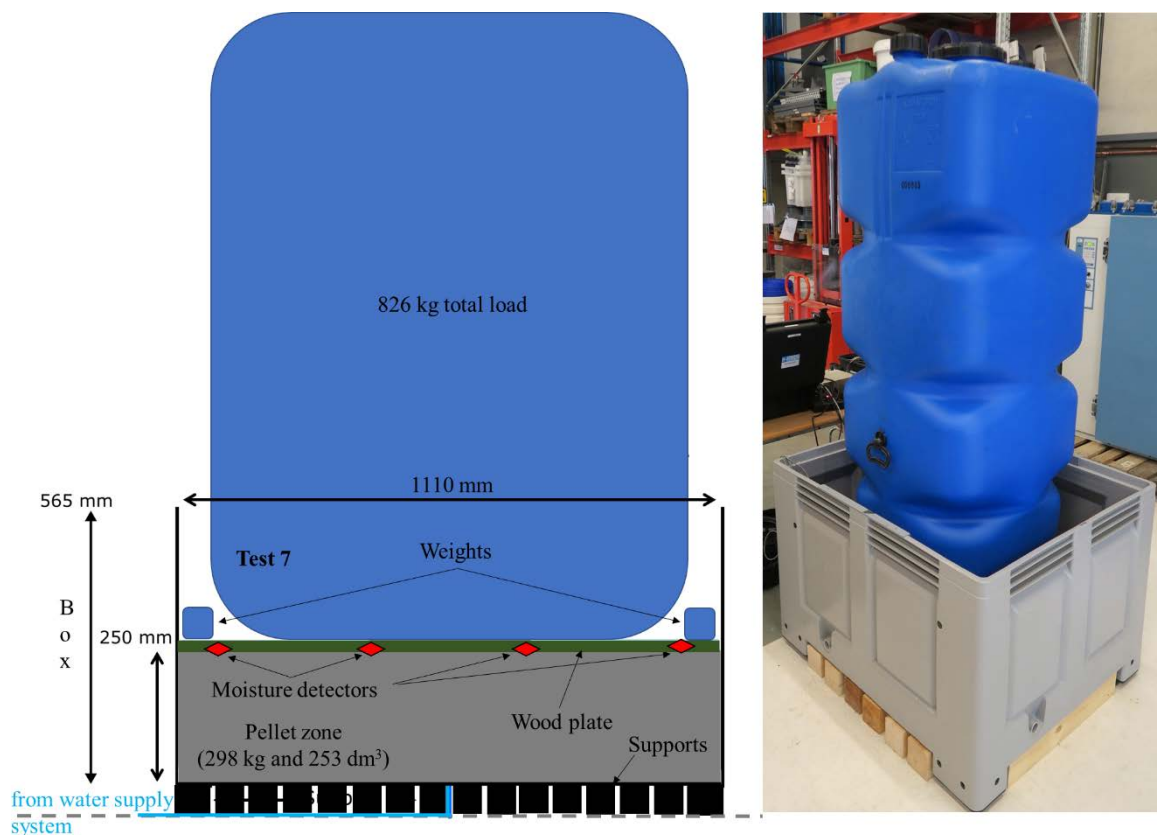


Figure 3-3. Cross-section schematic illustration of the test system (left) showing test setup, initial pellet volume dimensions, water inlet position and location of moisture detector sensors and photographic images (right) of floor wetting test 07. A surface load (826 kg) on the top of the pellet-filling was used in the test.

The inflow point in the bucket tests was located in the middle of a pellet filling. The ratio between the inflow rate and the pellet-filled volume was selected so that wetting would principally occur before the effect of confining walls or bottom would have to be considered. The goal was to achieve 3D wetting pattern without wall and floor contact and to determine the maximum downwards wetting length prior to upwards migration. In contrast, the inflow point in the box tests was located in the middle of the bottom of the pellet filling (underneath pellet material). The ratio between the inflow rate and the pellet-filled volume was selected so that wetting would occur without the effect of confining walls. The goal in the floor wetting test series was to achieve 3D wetting pattern without wall contact and to determine the wetting length along the floor before wetting goes upwards, piping channel forms to the surface and wetting happens along the pellet surface.

The inflow rate and the inflow pressure were registered in each test (Figure 3-4).

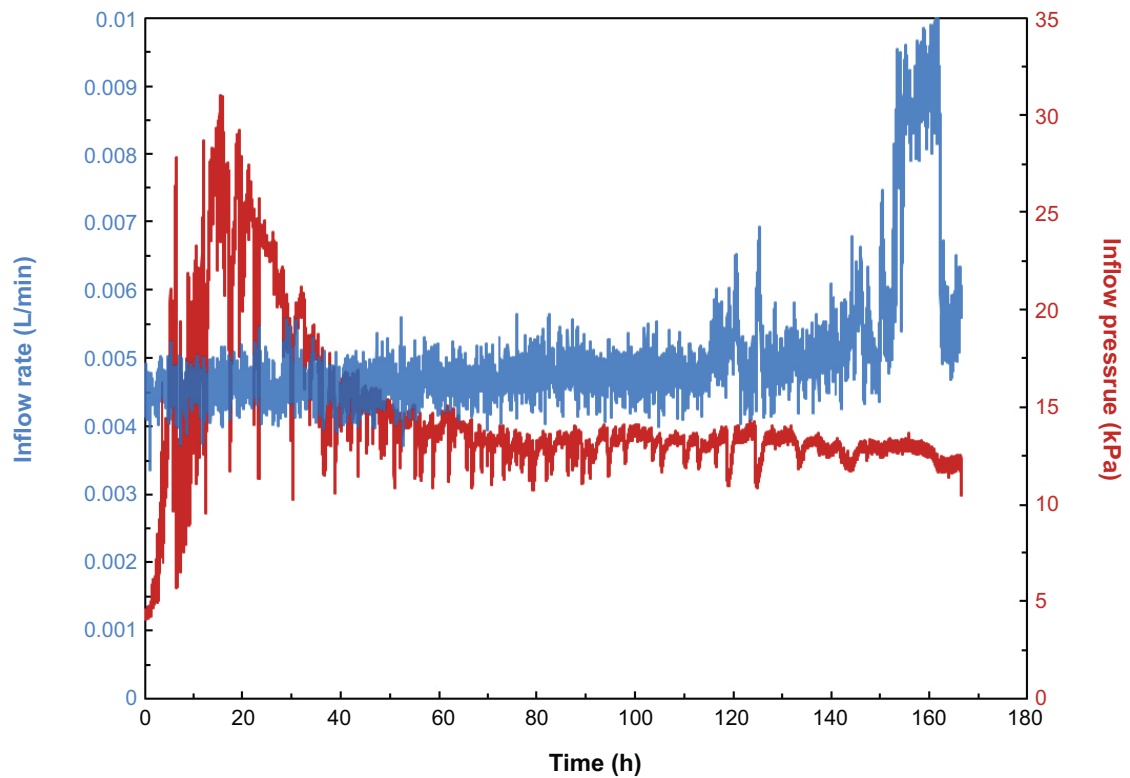


Figure 3-4. Total inflow rate (blue) and inlet pressure (red) in bucket test 02.

3.2 Wetting pattern

The water pumped into the test systems was dyed with blue and red colours during specific time periods in order to get a better understanding of water infiltration behaviour during the test. Areas dyed with these colours were revealed during the dismantling, and 3D wetting maps could be constructed from these results (Figure 3-5).

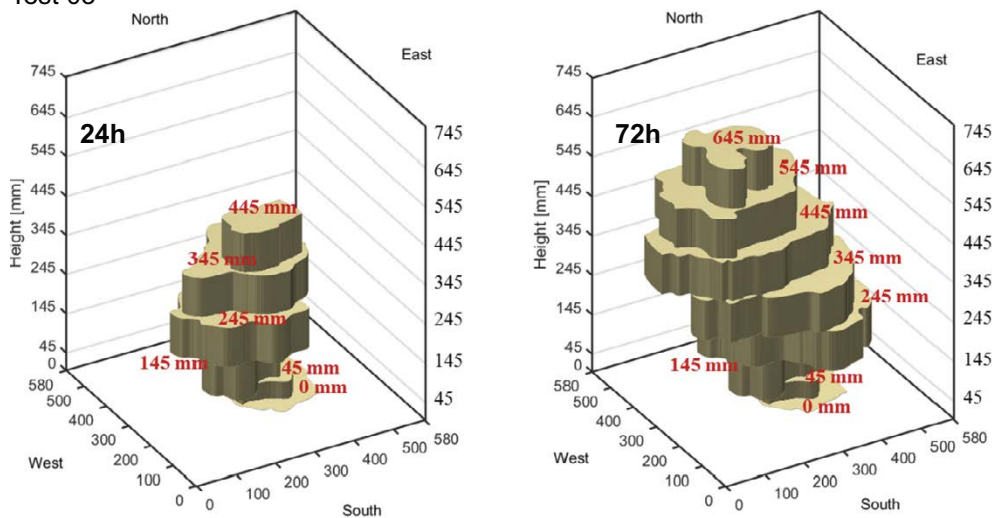
3.3 Task description

The modelling task description was initially formulated as:

- Use similar bucket/box setup geometry as in the experiment.
- Simulate wetting pattern and water content evolution, optionally also upheave of pellet surface.
- 1st phase: symmetric model, wetting evolution upwards/downwards/sideways in bucket and upwards/sideways in box.
- 2nd phase: randomize porosity/dry density distribution of pellets/use single pellets and packing, wetting evolution upwards/downwards/sideways in bucket and upwards/sideways in box.
- Key question: What kind of model is needed for capturing wetting caused by flow channels? Can it be implemented in THM codes, possibly in simplified form?

During the course of the task it became apparent how difficult it is to simulate these processes, and this meant that the work was mostly focused on the last point in this list.

Test 03



Test 06

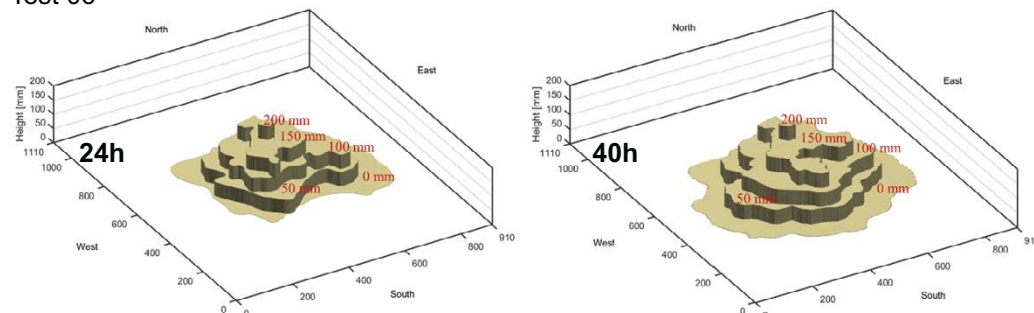


Figure 3-5. 3D qualitative wetting pattern images for test 03 (upper) and test 06 (lower) after 24 h (left) and at the end of the test (right).

4 Model contributions

This chapter presents a short overview of the different modelling contributions and their used codes and materials models, as well as a comparison of these material models. Due to the inherent complexity of the analysed problem, this evaluation has not included any compilation of model result, but rather a comparison of modelling approaches followed by the different teams.

4.1 Posiva/Elomatic

The model contribution presented by the Posiva team from Elomatic Oy was made using the StarCCM+ code (Aro et al. 2019).

Model description. The presented models, with 3D geometry, were based on the VOF (volume of fluid) method, in which the properties of the fluid are based on the mixture properties and no separate equations are required for different phases. In this case, the single phase is a mixture of water and air, for which properties like density and viscosity depend on the volume fraction of water, and an additional transport equation is added to track the volume fraction of water. The model does therefore not include any capillary action/osmotic forces, and no defined water retention curve, which means that the water transport is driven only by the applied pressure at the boundary and by gravity.

The fluid flow is based on equations for the *conservation of mass and momentum*, and also on a relation for the volume fraction of water. The momentum balance incorporates a term with the porous resistance (f_b):

$$f_b = P_V v_s + P_I v_s |v_s| \quad 4-1$$

where v_s is the fluid velocity. The two terms represent viscous and inertial parts, respectively, where the latter part is omitted. The factor in the viscous part (P_V) is defined as a function of the porosity (χ):

$$P_V = C_1 \chi^{C_2} \quad 4-2$$

The absorption rate and the rate by which the porosity decreases, is proportional to the volume fraction of water (α_w):

$$\frac{d\chi}{dt} = -a_w \alpha_w \quad 4-3$$

The reduction of the porosity and increasing porous resistance leads to the build-up of liquid pressure. And if this pressure reaches a certain limit (10 kPa), then there is a mechanism for channel formation. This means that a channel path is formed between the inlet, or the last end point of the previous path, and the nearest point in the outer surface of wetted area. The path is modelled as a region where the flow resistance is smaller than in the surrounding wetted area (Figure 4-1).

Outline of work. The first part of the report is devoted to different laboratory tests, i.e. wetting and swelling test, and flow resistance measurements. The development and the calibration of the model (regarding the parameters a_w , C_1 and C_2) is then presented. The last part presents results from different modelling cases from which the results can be compared with experimental data; i.e. bucket tests (included in this task), and box tests with wetting of pellets in a slot with dimensions 1 m \times 1 m \times 0.1 m. Finally, different model cases with wetting of the pellets-filled slot in a deposition hole is presented.

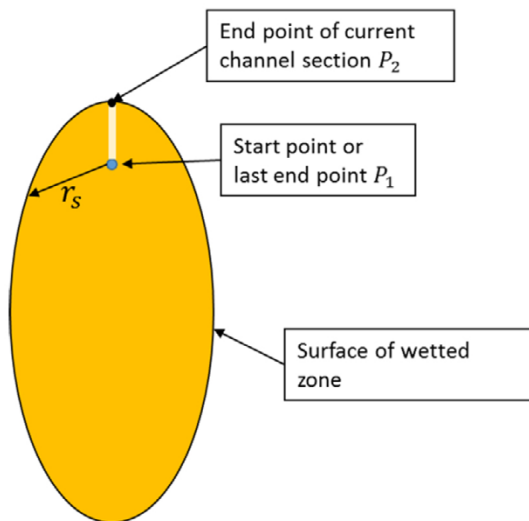


Figure 4-1. Channel formation in simulation model.

Results. The bucket tests were simulated with a conical model geometry. Results for two cases with different parameters were presented (Figure 4-2, upper left). None of the simulations matched the experimental data exactly (see Figure 3-5, upper), but the overall behaviour was fairly well captured. Two pellet box tests were simulated with two models with identical parameter sets but with different flow rates. Simulated wetted volume size and shape were roughly similar to the observation with the same flow rates fed into the box (Figure 4-2, lower left). The deposition hole models included bentonite pellets, bentonite blocks and a canister, but only the water transport in the pellets was simulated. The influence of injecting water from one of three different points along the outer boundary was investigated. In addition, the influence of five different flow rates, injected at a central injection point, was analysed. Results for two such cases are shown in Figure 4-2 (right). In general, the wetted volume was initially quite circular, but after a while the wetting was more directed upwards, especially for the highest flow rate.

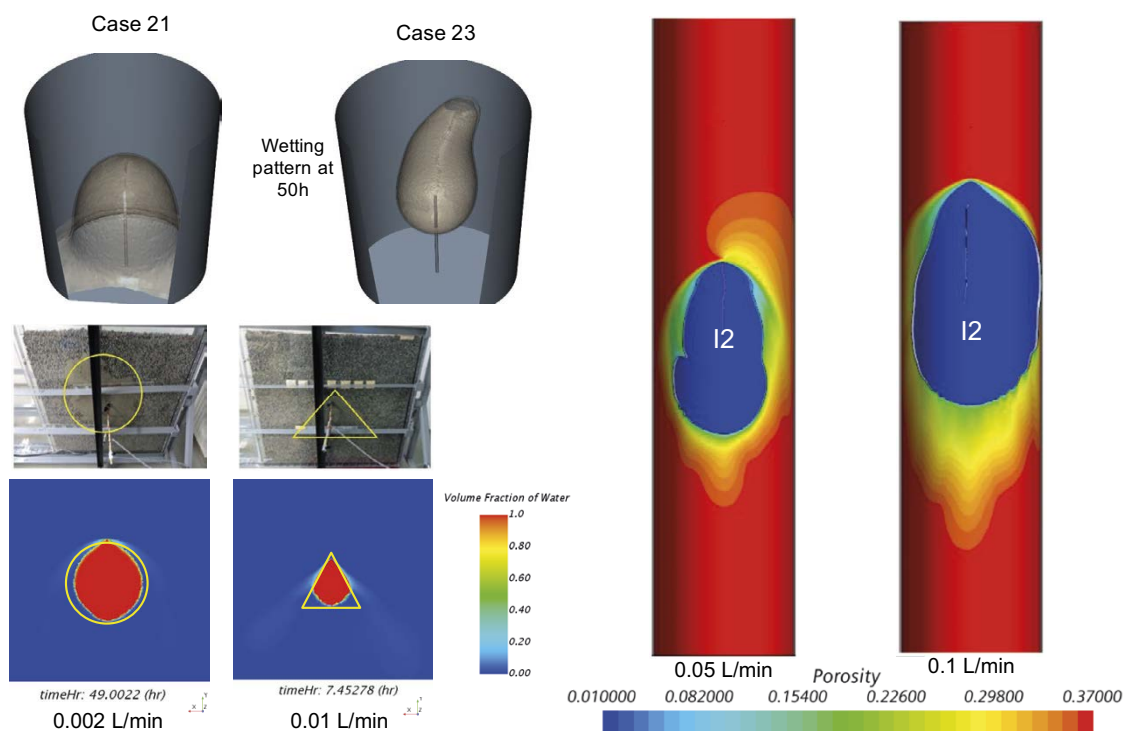


Figure 4-2. Model results from bucket test (upper left), pellets box (lower left) and a full-scale deposition hole (right).

4.2 NWS/Jacobs

The model contribution presented by the NWS team from Jacobs Clean Energy Limited was made using COMSOL Multiphysics (Wu et al. 2021).

Model description. The presented models, with 2D axisymmetric geometry, were based on a mass conservation equation combined with Darcy's law for unsaturated conditions, i.e. Richards equation. For the water retention curve, a modified van Genuchten curve was chosen:

$$S_e(P_l) = \left[1 + \left| \frac{P_l}{P_0} \right|^n \right]^{-m} \cdot \left[1 - \left| \frac{P_l}{P_d} \right| \right]^{k'} \quad n = 1/(1 - m) \quad 4-4$$

A water absorption rate was defined as:

$$W_e = W \phi^m S_e^m \quad 4-5$$

where W [$\text{kg}/(\text{m}^3 \cdot \text{s})$] is a constant, ϕ^m is macroporosity (0.423 initially), and S_e^m is effective saturation of the macroporosity. This water absorption leads in turn to a reduction of the porosity:

$$\phi^m(x, t) = \phi_0^m - \int_0^t \frac{W}{\rho} \phi^m(x, t) S_e^m(x, t) dt' \quad 4-6$$

where ϕ_0^m is the initial macroporosity and x is the position in the bucket. Finally, the permeability was defined as a function of the porosity:

$$k(x, t) = k_0 \left(\frac{\phi^m}{\phi_0^m} \right)^2 \quad 4-7$$

Outline of work. The first part of the report presents the development and tests of a hydraulic model, and includes a parameter study (regarding permeability and retention parameters), and an examination of the effect of a vertical variation in permeability. This part also included an analytical calculation of flow through a hollow sphere. The influence of water absorption was investigated in the second part, and this also included a test with a prescribed evolution of the porosity and the influence of this on the pressure evolution. In the third part the influence of different mechanical models (i.e. a linear elastic model, an elastoplastic model with a Drucker Prager yield surface, and a modified Cam-clay model) was investigated. The goal of these models was to simulate the measured heave in bucket Test 02. The final chapter presents an analytical model for upward flow, which was an attempt to provide a conceptual explanation for the increase in permeability found to coincide with the heaving of the pellets.

Results from the hydraulic model with water absorption is shown in Figure 4-3. The water absorption rate (W) was calibrated so that the absorbed water volume (27.5 litres) was equal to the average heave observed in bucket Test 02. Among the mechanical models, the linear elastic model tended to result in a fairly correct heave, but this model also displayed high tensile stresses in the dry part of the pellets. In contrast, the case with the modified Cam-clay model resulted in very low tensile stresses, but it was not possible to complete the calculations due to numerical difficulties (see Figure 4-4).

The analytical model for upward flow addresses a simple 1D system with a tube sealed at the bottom and containing a permeable disk that is free to move within the tube and has some load upon it. Water is injected at a fixed rate into the tube at its base, and water flowing through the disk is removed from the top of the disc. Different flow conditions are then considered among which the most important is a case in which the injection rate is high in relation to the permeability of the disk. The water pressure needed to drive all of the injected water through the permeable disk would then be sufficient to lift the disk (and its load) off the base of the tube against gravity. The actual water pressure would however be lower, since some fraction of the inflow would contribute to the filling of increasing volume beneath the disk. The evolution of height of the base above the base of the disk (H) can then be described by the following function:

$$H(t) = H_0 + \frac{C}{\alpha} (1 - e^{-\xi t}) + \left(\frac{Q_{in}}{A} - \frac{M_L g k}{A \mu d} \right) \cdot t \quad 4-8$$

where the first term is the initial value, the second is a transient during which the pressure reaches the pressure level to lift the load, and the third is a linear increase with time. A similar model for downward flow was outlined by replacing the lifting of the load with the compression of the medium underneath. It is suggested that these two models can explain some of the features of the tests, especially that the movements of the pellets above and beneath the inlet may influence the effective permeability of the pellets medium.

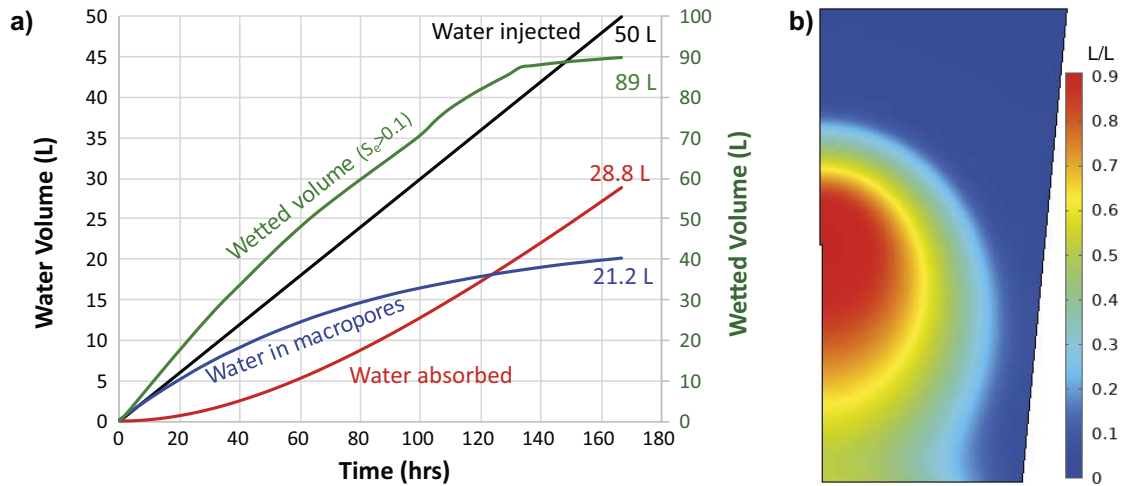


Figure 4-3. Model results for case with water absorption: evolution of absorbed water, water in macropores and injected volume (left), negative of total absorbed water per litre after 166.5 hours.

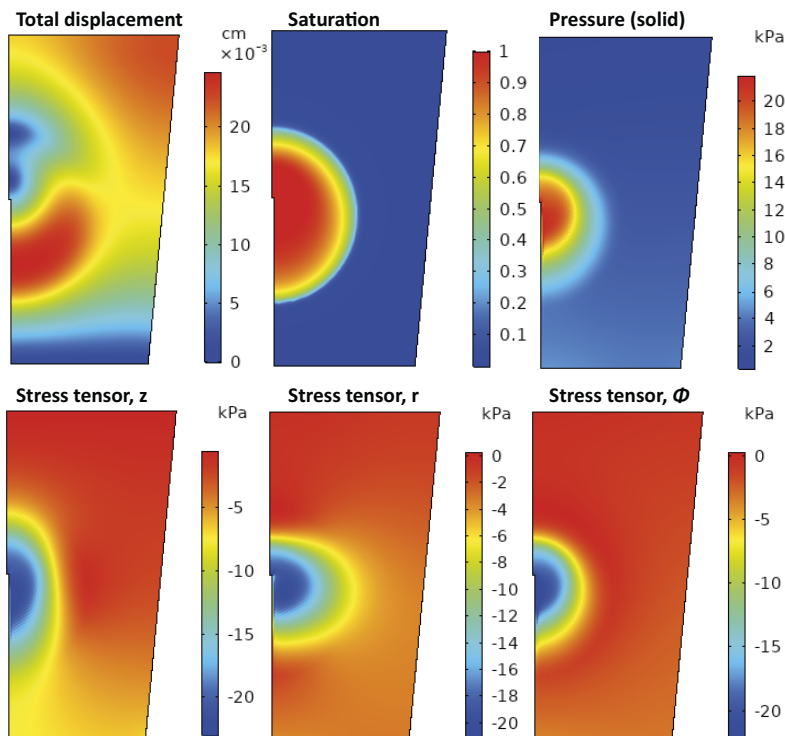


Figure 4-4. Model results for case with modified Cam-clay model after 17 hrs.

4.3 SKB

The model contribution presented by the SKB team was made using COMSOL Multiphysics (Eriksson 2019, 2020).

Model description. The presented models were based on a 2D framework with two porosities; one for free water and one for clay water. The water transport in the *free water* is described with a multi-phase Darcy's equation, for which the permeability was translated from the linear term of the Ergun equation. This permeability (κ) is a function of the gas porosity (φ_a) which in turn is equal to the porosity multiplied with one minus the saturation degree ($n(1 - S_M)$):

$$\kappa(\varphi_a) = \frac{4 \cdot r_0^2 \cdot \varphi_a^3}{c_1 \cdot (1 - \varphi_a)^2} \quad 4-9$$

The water retention curve is based on Brooks-Corey:

$$p_l(S_M) = p_{atm} + p_{ec} \cdot (1 - S_M)^{-1/\lambda} \quad 4-10$$

and also, the relative permeability is based on Brooks-Corey:

$$\kappa_{r1}(S_M) = S_M^2 \cdot [1 - (1 - S_M)^{1+2/\lambda}] \quad 4-11$$

This approach utilizes the description for the non-wetting fluid in the two-phase description for the water. This means that the liquid pressure is always higher than the gas pressure. For the *clay water*, the transport is described by the Richards equation, and also with a water retention curve, in which the suction is defined as a function of the water content and in which also the hysteresis effects are included. The exchange between the two porosities is described by a one-way absorption coupling with an absorption rate which is proportional to the suction value of the clay water (p_s):

$$c \cdot p_s \cdot \theta(S_M) \quad 4-12$$

The model incorporates a mechanism for channel formation. This is performed by adding a channel segment each time the water pressure exceeds a defined threshold value. The direction of each new segment is set to be the same as the direction of the maximum flow velocity. This is implemented by updating the geometry, and the procedure for this is controlled with a Java program.

Outline of work. The model is described in two reports (Eriksson 2019, 2020). The first covers the work on subtask A and C and also all parts of this new model, except for the procedure with channel formation which is described in the second report. The model has been applied for simulation of: i) the general behaviour of water transport at different flow rates; ii) two pellets box tests with dimensions 1 m × 1 m × 0.05 m; and iii) one experiment which represents a 1 m high section of a deposition hole. The last test was modelled by using the 2D pellets model with channel formation as a boundary condition for a 3D hydromechanical model (see Eriksson 2020).

Result. Simple tests in which the inflow rate is varied demonstrate that the model is able to capture the behaviour with downward directed flow at high flow rate 0.1 l/min, upward directed at 1 ml/min, and symmetric wetting patterns for very low flow rates (Figure 4-5). The overall behaviour of the wetting in the pellets box tests, with upward directed wetting for a flow rate of 0.01 l/min and downward directed at 0.1 l/min, was also well-captured (Figure 4-6).

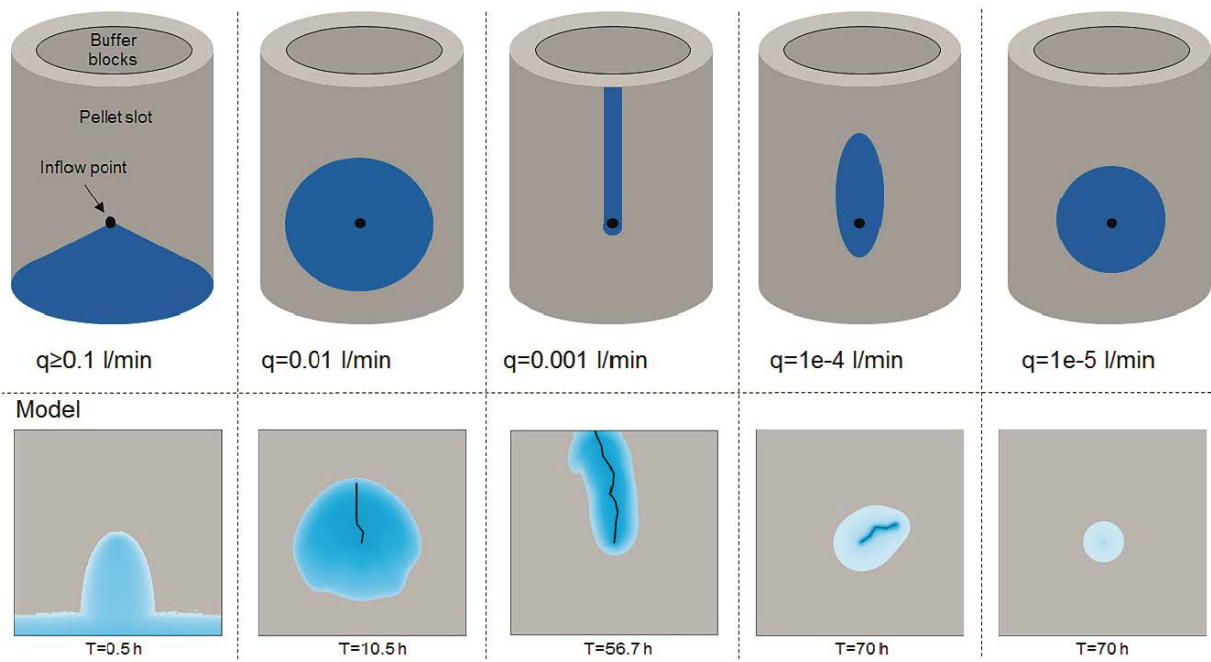


Figure 4-5. Model results illustrating the influence of different flow rates (bottom row) compared to the conceptual model presented by Börjesson et al. (2015) (top row).

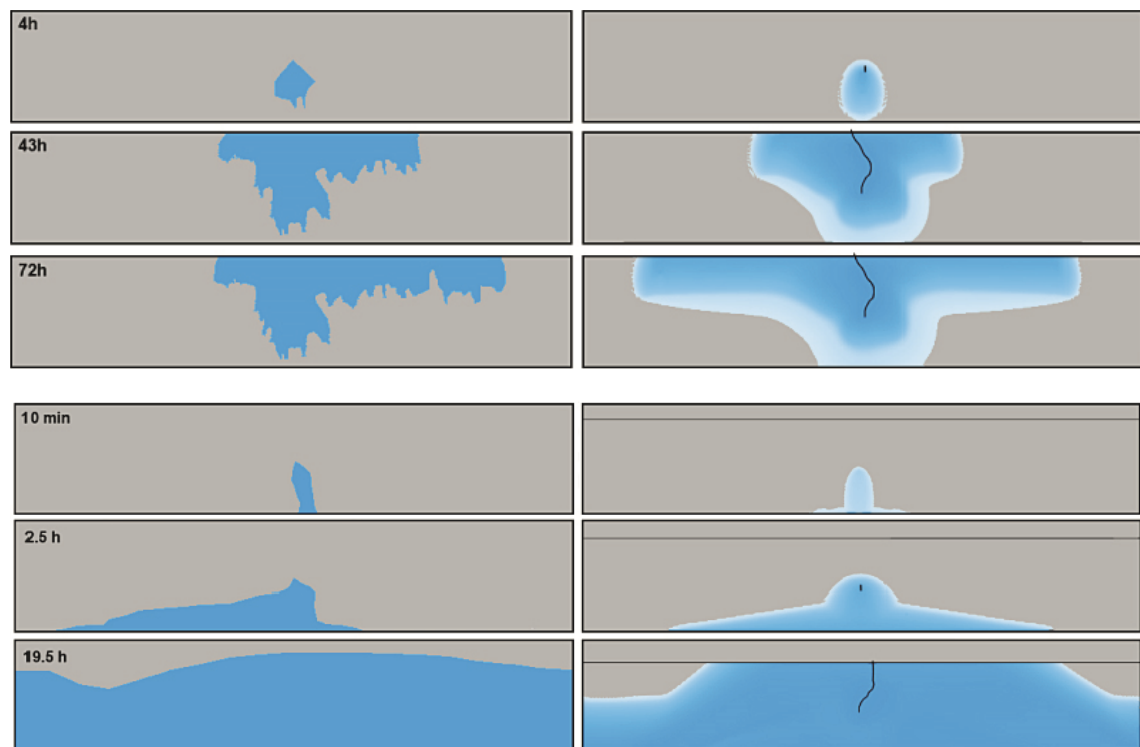


Figure 4-6. Pellets box tests. Model results (right) and experimental results (left) for three times and two flow rates; 0.01 l/min (upper) and 0.1 l/min (lower).

4.4 SKB1/Claytech

The model contribution presented by the SKB1 team from Clay Technology was made using COMSOL Multiphysics (Kristensson et al. 2022).

Model description: The presented models were based on a 2D framework with three pore spaces, denoted macro, meso and micro voids. The description of the water transport of the macro voids (e_M) was inspired by the model presented by Eriksson (2020), especially regarding the water retention curve:

$${}^M S_l = 1 - \left(\frac{P_M - s_M}{P_M} \right)^{-\lambda_M}, P_M = 1300 \text{ Pa}, \lambda_M = 0.75, \quad 4-13$$

where s_M is the suction value of the macro voids. The water transport followed Darcy's law. The dependence of the macro porosity (ϕ_M) on the permeability was described with the Kozeny-Carman relation:

$$\kappa_0 f(\phi_M) = fact_{\kappa} \frac{d^2}{180} \frac{\phi_M^3}{(1 - \phi_M)^2} \frac{(1 - \phi_M^0)^2}{(\phi_M^0)^3} \quad 4-14$$

A new relative permeability function was adopted with the goal to minimize the mobility of the macro pore water for low saturation degrees:

$$g({}^M S_l) = \frac{1}{1 + \exp\left(\frac{a - {}^M S_l}{b}\right)}, a = 0.3, b = 0.03. \quad 4-15$$

The meso voids (e_m), was defined as totally dry. The micro voids (e_μ) was defined as water saturated. The relationship between e_μ and the suction value of the micro voids (s_μ) was defined as:

$$\frac{e_\mu}{e} = \left(1 + \left(\frac{\max(s_\mu, 0)}{P_\mu} \right)^{\frac{1}{1-\lambda_\mu}} \right)^{-\lambda_\mu}, P_\mu = 0.4717 \text{ MPa}, \lambda_\mu = 0.25, \quad 4-16$$

For simplicity, no water transport within the micro void framework was enabled. The rate of absorption from the macro to the micro voids is proportional to the degree of saturation of the macro pores and the suction value of micro pores.

$$\dot{\alpha} = \dot{\alpha}_0 \text{ step}\left({}^M S_l - {}^M S_l^0\right) s_\mu. \quad 4-17$$

The absorption leads to the increase of the micro void ratio and the decrease of the macro and the meso voids ratios. The ratio between the meso and the macro pores is assumed to be constant, in order to define the relative evolution of the three pore spaces.

Finally, an algorithm for channel formation was implemented by using the "state variable" feature of COMSOL Multiphysics. A variable denoted "pipe" is defined, and each time the pressure in the last channel segment reaches a threshold value a new segment is added to the previous segments. This is represented by increasing the pipe variable from 0 to 1 in all locations within this segment. The orientation of each new segment is the same as the gradient of s_M at the point of origin of this segment (Figure 4-7). The pipe variable will influence the permeability field by adding a term $\kappa_{pipe} = pipe \cdot \kappa_{pipe}$ ($\kappa_{pipe} = 5 \times 10^{-13} \text{ m}^2$):

$$\kappa = \kappa_0 \kappa_{rel} + \kappa_{pipe} \quad 4-18$$

Outline of work. The model is described in Kristensson et al. (2022). The first part of the report is devoted to a presentation of the theory and a description of the model and how this is implemented in COMSOL Multiphysics. Two test simulations are then presented in which the overall behaviour of the model is investigated; the first regarding the formation of channels, and the second regarding influence of the inflow rates.

Result. The first test simulation illustrates that the algorithm for an upward moving channel formation is working, see Figure 4-8, although results also revealed that some part of the formulation seems to be improper regarding the channel orientation. The second test simulation shows that the formulation can capture different wetting modes for different inflow rates, especially for high inflow rates with pronounced downward directed wetting.

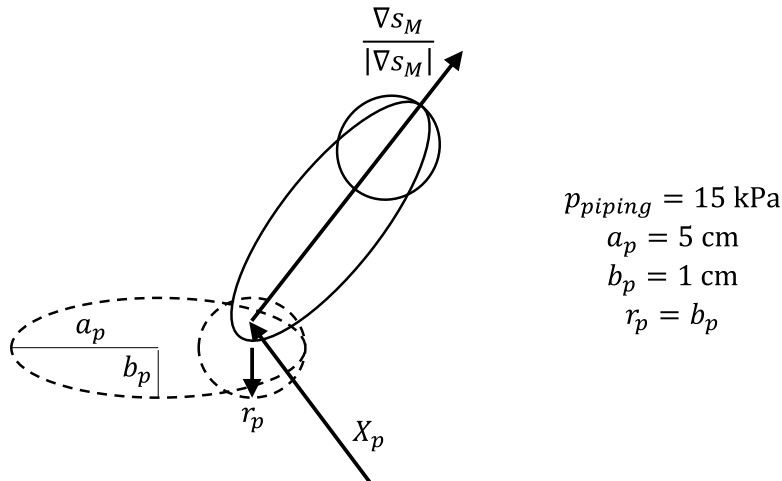


Figure 4-7. Geometry of the piping channel section and the pipe formation parameters.



Figure 4-8. Total saturation and pipe state variable after 80 h in the piping channel formation test.

4.5 Comparison of material models

A compilation of all the model contributions is presented in Table 4-1. It can be noted that all teams used the code COMSOL Multiphysics, except for the Posiva team who instead used the StarCCM+ code.

The geometries used by the different groups were quite different: the Posiva team used a 3D geometry, the NWS team used a 2D axisymmetric geometry whereas the SKB and SKB1 teams used plane 2D geometries. The latter type of geometry implies that a depth is assumed; in the SKB pellets box model this was 5 cm, while the SKB1 team used a depth of 1 m.

All contributions have included some description of the water transport in the pore systems between the pellets, here denoted the Macro flow. The three teams from NWS, SKB and SKB1, have all used Darcy's law and some form of water retention curve, and both the SKB and the SKB1 used unusual water retention curve with which the liquid pressure exceeded the gas pressure. In contrast, the Posiva team used two-phase flow description in which no water retention curve was employed.

Only the SKB and the SKB1 teams had a representation of water transport in the micro voids, but in the case of SKB1 this was set to zero in order to simplify the problem. All teams included some form of water absorption which in turn reduced the permeability and thereby sealed the macro flow. Three of the teams (Posiva, SKB and the SKB1 team) included some representation of piping and channel formation.

Table 4-1. Constitutive relations used in the different contributions.

| Constitutive equation | POSIVA/Elomatic | NWS/Jacobs | SKB | SKB1/Claytech |
|-----------------------|--------------------------------------|--------------------------------|--|--|
| Code | StarCCM+ | COMSOL Multiphysics | COMSOL Multiphysics | COMSOL Multiphysics |
| Geometry | 3D | 2D axisymmetric | 2D (depth 5 cm) | 2D (depth 1 m) |
| Macro flow | Two-phase flow No retention curve | Darcy's law Retention curve | Darcy's law Retention curve ($p_l > p_g$) | Darcy's law Retention curve ($s < 0$) |
| Micro flow | No | No | Yes | Yes (but set to zero) |
| Uptake & sealing | Yes | Yes | Yes | Yes |
| Piping | Yes, Changed flow resistance | No | Yes, Changed geometry | Yes, Changed permeability |

5 Evaluation

This chapter presents comparisons and evaluations of different parts of the constitutive models and parameter values used by the different teams, and how these features influence the behavior of the different models.

5.1 Macro retention

A compilation of the retention curves for the macro voids used by the different teams is presented in Figure 5-1. Two curves from the SKB1 team are shown. The one denoted #1 is defined as:

$${}^M S_l = \min \left(1, {}^M S_l^{ref} + (1 - {}^M S_l^{ref}) \exp \left(\frac{-\max(s_M, -1000 \text{ Pa})}{P_M} \right) \right) \quad 5-1$$

where $P_M = 300 \text{ Pa}$ and ${}^M S_l^{ref} = 0.01$, and this was the original curve used by that team. The one denoted #2 was the final curve (see Section 4.4), which was identical with the one proposed and used by the SKB team. The curves by NWS and SKB1 (#1) are quite similar and both display a conventional outline with positive suction values, whereas the SKB (and SKB1 #2) curve is quite different with negative suction values, which means that the liquid pressure exceeds the gas pressure. No retention curve was used in the model presented by the Posiva team.

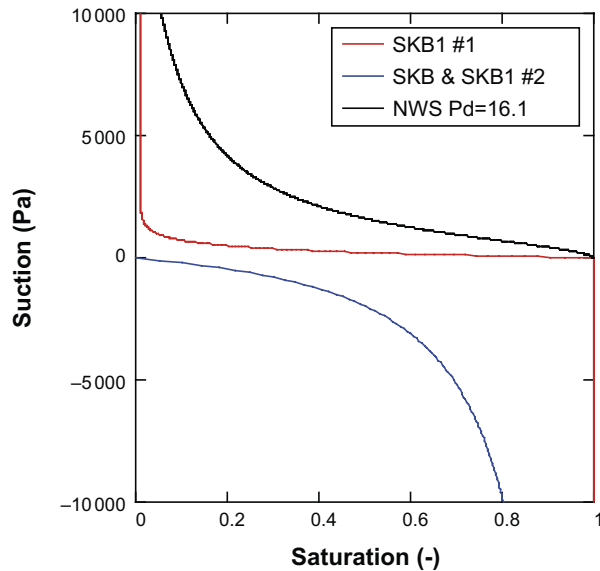


Figure 5-1. Water retention curve used by the teams from NWS, SKB and SKB1.

5.2 Saturation fronts

The choice of water retention curve appears to influence the numerical stability of the numerical model. An analysis of such a potential influence can be based on the notion of saturation fronts. This is here defined as a section, with a certain length L , through which the water flux (q) is constant, with an initial pressure level (P_0) at the left side, and with a boundary pressure (P_{BC}) at the right side. The permeability is assumed to be a function of the pressure. From this a relation between the coordinate (x) and the liquid pressure (P) can be derived, and together with a retention curve, a saturation profile can be calculated.

The analysis is based on Darcy's law:

$$q = -\frac{k(P_l)}{\mu} \cdot \frac{dP_l}{dx} \quad 5-2$$

This is evaluated by integrating x from 0 to X on the left side and P_l from P_0 to $P(X)$ on the right side:

$$\mu q \int_0^X dx = - \int_{P_0}^{P(X)} k(P_l) dP_l \quad 5-3$$

Since q is constant, the following general relation between x and P can then be derived:

$$x(P) = \frac{\int_{P_0}^P k(P_l) dP_l}{\int_{P_0}^{P_{BC}} k(P_l) dP_l} L \quad 5-4$$

This method has been applied to the permeability relations and water retention curves presented by SKB and SKB1 (#1). For the latter, the following relative permeability relation was used together with the retention curve (Equation 5-1):

$$g(M S_l) = M S_l^\beta, \quad \beta = 4 \quad 5-5$$

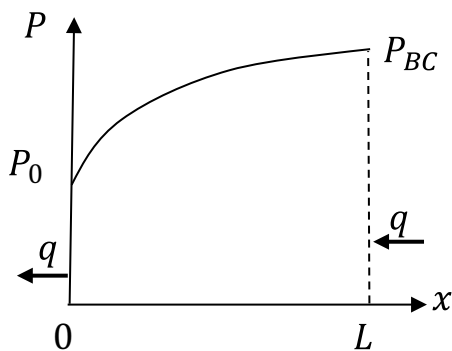


Figure 5-2. Pressure profile in stable saturation front with equal in- and outflow.

The results are presented in Figure 5-3. The left graph shows the results for the SKB case; with the *relative* pressure varying from entry capillarity value (P_{ec}) 1 300 Pa to the boundary pressure of 15 kPa, which together with retention curve means that the saturation varies from 0 to 0.85. Both distributions generally display smooth shapes. The centre lower graph shows the results for the SKB1 #1 case; with a liquid pressure varying from -6 MPa (chosen for convenience) to +15 kPa, and with the saturation varying from 0 to 1. Both profiles generally display very sharp shapes, and this indicates that the conventional water retention curve with large negative pore pressure leads to numerical difficulties. The right graph shows the results for the SKB1 #2 case; with a “negative suction value” varying from 200 Pa to 15 kPa, with the saturation varying from 0.1 to 0.85. As with the SKB case, both profiles display smooth shapes.

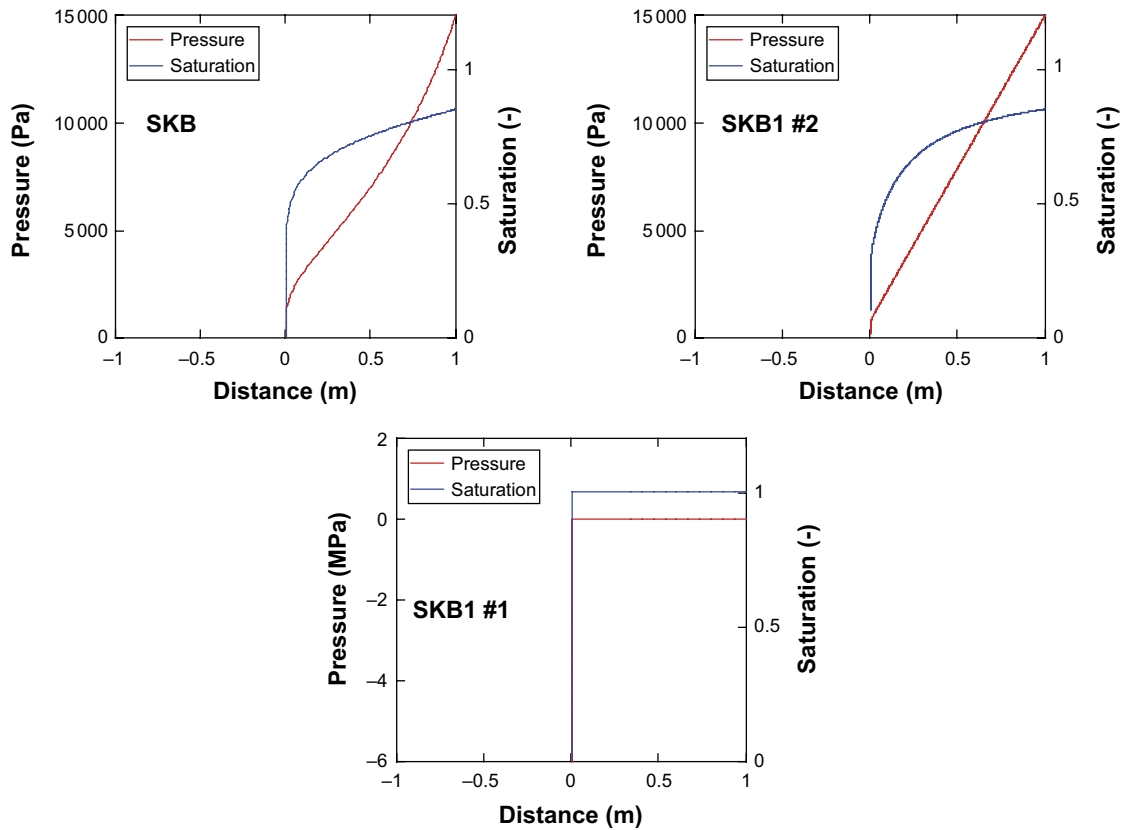


Figure 5-3. Saturation fronts resulting from three sets of retention and relative permeability relations.

5.3 Permeability relations

All modelling teams have used different permeability relations and how the porosity influences this property. A compilation of these relations is presented Figure 5-4. The Posiva team did not employ the Darcy's law, but rather a momentum balance which incorporates a term for the porous resistance (Equation 4-1). The ratio between the (dynamic) viscosity and the viscous part (P_V) of this porous resistance should be analogous to a permeability:

$$k_{Posiva} = \frac{\mu}{C_1 \chi C_2} \quad 5-6$$

Two different parameter values for C_1 was used: 10000 and 300000. For the teams from NWS, SKB and SKB1, the permeability relations (Equations 4-7, 4-9 and 4-14) were used. It should be noted that different teams used different porosity definitions; Posiva: χ , NWS: ϕ , SKB: ϕ_a and SKB1: ϕ_M (see Chapter 4). It can also be noted that the permeability relations used by the different teams display very different values. The highest level is found in the SKB model, with a permeability in the order of 10^{-6} m^2 , whereas the lowest level (six orders of magnitudes lower) is found for the NWS model. Values for the relations used by the Posiva and SKB1 teams are found within this span. A tentative explanation for this large span is given in the next section.

5.4 Absorption rates

All modelling teams have also used different expressions for calculating the rate of absorption. A compilation of these expressions is given in Table 5-1 together with an estimate of the maximum value of each model with a common unit of $\text{kg}/(\text{s} \cdot \text{m}^3)$. The rates for the models by both SKB and SKB1 are proportional to the suction value of the micro pores. The absorption rate in the Posiva model is expressed as a time derivative of the porosity which is proportional to the volume fraction of water, with the parameter a_w as a constant of proportionality (see Equation 4-3). The product of this constant and the density of water yields a quantity with the unit of $\text{kg}/(\text{s} \cdot \text{m}^3)$. For the NWS model, the rate is described as proportional to the porosity and the degree of saturation. As with the permeability relations, it can be noted that the absorptions rates used by the different teams display very different values. The highest level is found in the SKB model, with a rate in the order of $1 \text{ kg}/(\text{s} \cdot \text{m}^3)$, whereas the lowest level (three orders of magnitudes lower) is found for the NWS model. Values for the expressions used by the Posiva and SKB1 teams are found within this span.

Table 5-1. Compilation of absorption rates used by the different contributions.

| Team | Definition | Maximum value $\text{kg}/(\text{s} \cdot \text{m}^3)$ |
|--------|---|--|
| SKB | $c \cdot p_s \cdot \theta(S) \sim 12 \times 10^{-8} \times 20 \times 10^6 \times 1$ | 2.4 |
| Posiva | $a_w \cdot p_w \sim 2.5 \times 10^{-4} \times 10^3$ | 0.25 |
| SKB1 | $\dot{a}_0 ({}^M S_I - {}^M S_I^0) S_\mu \sim 10^{-3} \times 1 \times 60 \text{ MPa}$ | 0.06 |
| NWS | $W \phi S_e \sim 2.3 \times 10^{-3} \times 0.66 \times 1$ | 0.0015 |

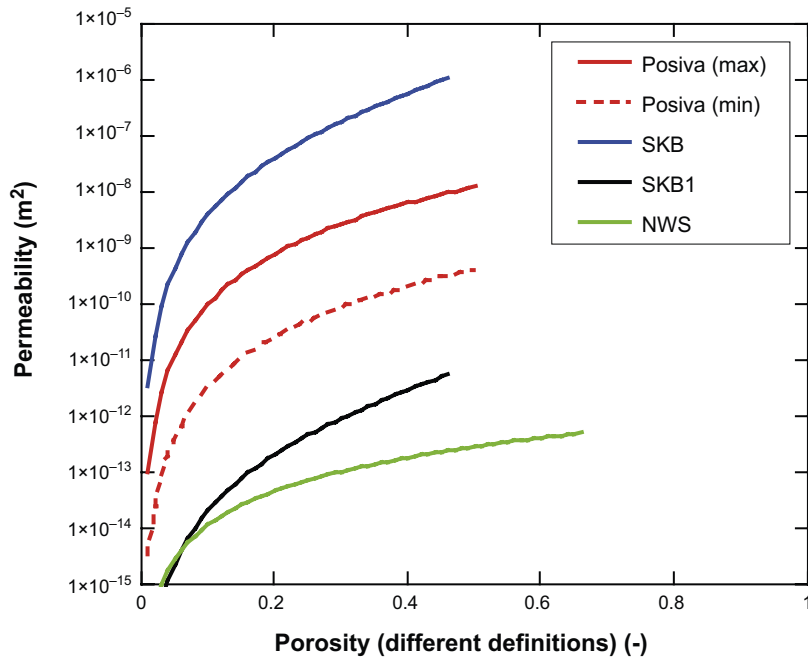


Figure 5-4. Compilation of permeability relations used by the different teams.

A relationship between the adopted values for the absorption rate and the permeability can be tentatively analysed with a simple water mass balance in which the storage term is constant:

$$\frac{dq}{dx} = -\frac{a}{\rho_w} \quad 5-7$$

q is the flux and a is the absorption rate. A combination of this with Darcy's law (Equation 5-2) yields the following expression:

$$\frac{d}{dx} \left(\frac{k(P_l)}{\mu} \cdot \frac{dP_l}{dx} \right) = \frac{a}{\rho_w} \quad 5-8$$

This indicates that a decrease in the permeability requires that the absorption rate also has to be decreased in order to preserve the same pressure gradient. For instance, if a relatively low value for the permeability for some reason is adopted during the calibration process, then it can be anticipated that a relatively low absorption rate also has to be adopted in order to obtain a sought pressure evolution. This can therefore give a tentative explanation for the large difference between the permeability values and absorption rates presented by the different teams. The reason why the permeability span in Figure 5-4 is three orders of magnitude larger than the absorption rate span in Table 5-1 is however not known. The quite large difference in the geometry between the different contributions (see Table 4-1) could possibly have some influence on these differences.

5.5 Channel pressure

The inlet pressure in many of the pellet wetting tests generally displays a rapid increasing trend in the beginning after which it reaches a peak value, and after that it decreases to a more stable level (e.g. Figure 3-4). A tentative explanation for this behaviour was proposed by the NWS team, and this was the idea behind the analytical model for upward flow (see Section 4.2 and Equation 4-8). An illustration of the proposed mechanism is shown in Figure 5-5 (left). The pellets may be separated by the upward flowing water, and this could in turn lead an increasing effective permeability.

An alternative explanation for the inlet pressure evolution can be sought in the notion that the water transport mainly occurs through a channel and that the flow resistance thereby can be described by Hagen-Poiseuille equation, which can be rearranged as:

$$L = \frac{\pi \cdot \Delta P \cdot R^4}{Q \cdot 8 \cdot \mu} \quad 5-9$$

where ΔP is the pressure difference along the channel, R is the channel radius, Q is the flow rate, μ is the viscosity and L is the channel length. An example of this is shown in Figure 5-5 (right) for a case with $Q = 0.005$ L/min and R increasing from 0.15 to 0.3 mm. This could explain a trend with ΔP increasing to 30 kPa after which it decreases to 10 kPa at the same time as L increases from 0 to 0.3 m.

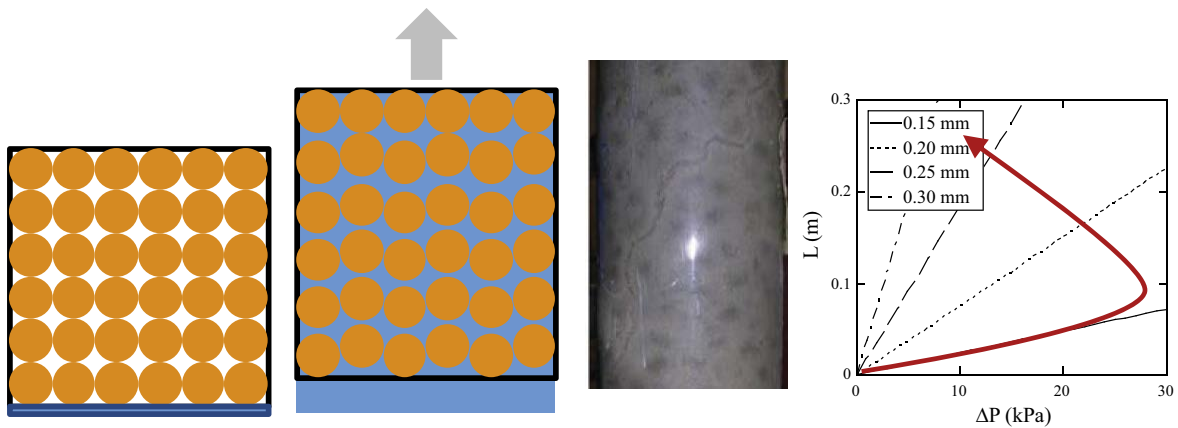


Figure 5-5. Tentative explanations of reduction in channel pressure: through separation of upward moving pellets leading to increasing effective permeability (left); and through reduced flow resistance through channel due to increased radius (right).

5.6 Channel formation

A simple illustration of approaches for determining the orientation of new channel segments is shown in Figure 5-6. The SKB team adopted a method in which the new segment was oriented in the same direction as the maximum flow rate. The SKB1 team chose a similar approach in which new segments were oriented in the direction of the suction gradient. The Posiva team, in contrast, adopted a quite different approach in which the direction with the shortest distance to dry material, unaffected by wetting, was chosen.

5.7 Comments

The presented comparisons and evaluations show that the different models display quite large differences, especially regarding the used water retention curves, the permeability values for the macroscopic porewater, and the absorption rate for this porewater. The differences regarding permeability and absorption can to some extent be explained through an analysis of the role of these properties in the water mass balance, and also the difference in geometry of the contributions (2D, 2D axisymmetric or 3D) may contribute to these.

Still, one feature which was used by all models was the role of the absorption of the macroscopic porewater. From this followed a general permeability reduction for this porewater, and from this it was possible to simulate an increasing water pressure at the water inlet.

A second feature, used by several teams, was the absence of a conventional water retention curve for the macroscopic porewater which defines the liquid pressure as lower than the gas pressure (one team did not use any water retention curve). This approach appears to make the simulation of the transport of macroscopic water numerically more stable.

Finally, several teams have implemented a representation of channel formation in their models. This can be made in different ways, through modification of the permeability field or of the geometry. Such modifications rely on used codes and the options that are available in these codes.

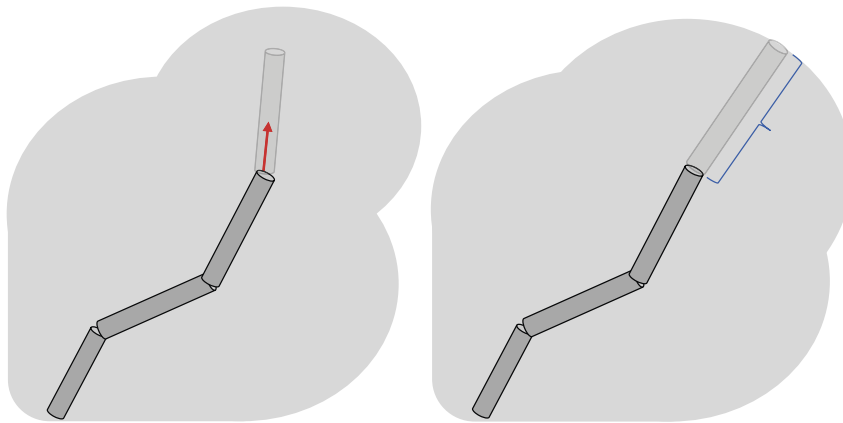


Figure 5-6. Schematic illustration of two approaches for orientation of new channel segments; with the same direction as the maximum flow rate, or suction gradient (left), and the direction with the shortest distance to dry material (right).

6 Outlook for further developments

6.1 Introduction

Results from subtask B show that the very peculiar wetting patterns associated with bentonite pellets can be mimicked with numerical models. Among the different contributions, especially the Posiva and the SKB teams have presented very promising results. However, a significant departure from the conventional descriptions of hydromechanical processes in bentonite seems to be needed in order to mimic these wetting patterns. It may therefore be useful to reflect upon and evaluate the role of different processes involved in the water saturation of buffer and backfill materials in deposition holes and tunnels. Such an evaluation is presented in this chapter and it's arranged by discussing three topics: i) dismantling data from the Prototype repository; ii) a tentative description of the water saturation processes as being composed of three flow systems and four phases, and iii) a discussion of the hydromechanical interaction between the buffer/backfill-system and the near-field rock.

6.2 Field experiment data

The outer section of the Prototype experiment was dismantled in 2011 and consisted of: i) a 23 m long tunnel section filled with a backfill material consisting of a mixture of crushed rock and bentonite (70/30) and; ii) two deposition holes with canister and buffer installed as block and pellets. An extensive and detailed analysis regarding the water content and the density of the buffer was performed during the course of the dismantling of this outer section (Johannesson 2014). These measurements showed that the buffer had reached high saturation degrees in almost all parts except in the central parts of the cylinder below the canisters, and in the two cylinders above the canisters. Moreover, the distribution of the water content (Figure 6-1) and the dry density in some sections in both deposition holes (Dh5 and Dh6) showed that the wetting and the swelling in one direction was much larger than in the opposite direction, and that this pattern was more pronounced in the upper part of the buffer. This may be correlated with the mapped fractures in the case of Dh5, but this does not seem to be a likely explanation for Dh6. Instead, the results from the upper 5–6 blocks in both depositions holes clearly indicate that water to some extent have entered from the tunnel, and that water conducting channels were formed in the pellets-filled slot. This notion is also supported by the buildup of pore pressures throughout the backfill with approximately 1 MPa during the last three years of operation. The distribution of water content and dry density in the backfill in the outer section also displayed some significant heterogeneities, and the highest water contents and the lowest dry density values were generally found close to the tunnel ceiling (Figure 6-1). This therefore indicates that a water conducting channel was formed along the ceiling and that a high pore pressure in this may have contributed to a downward displacement of the backfill material.

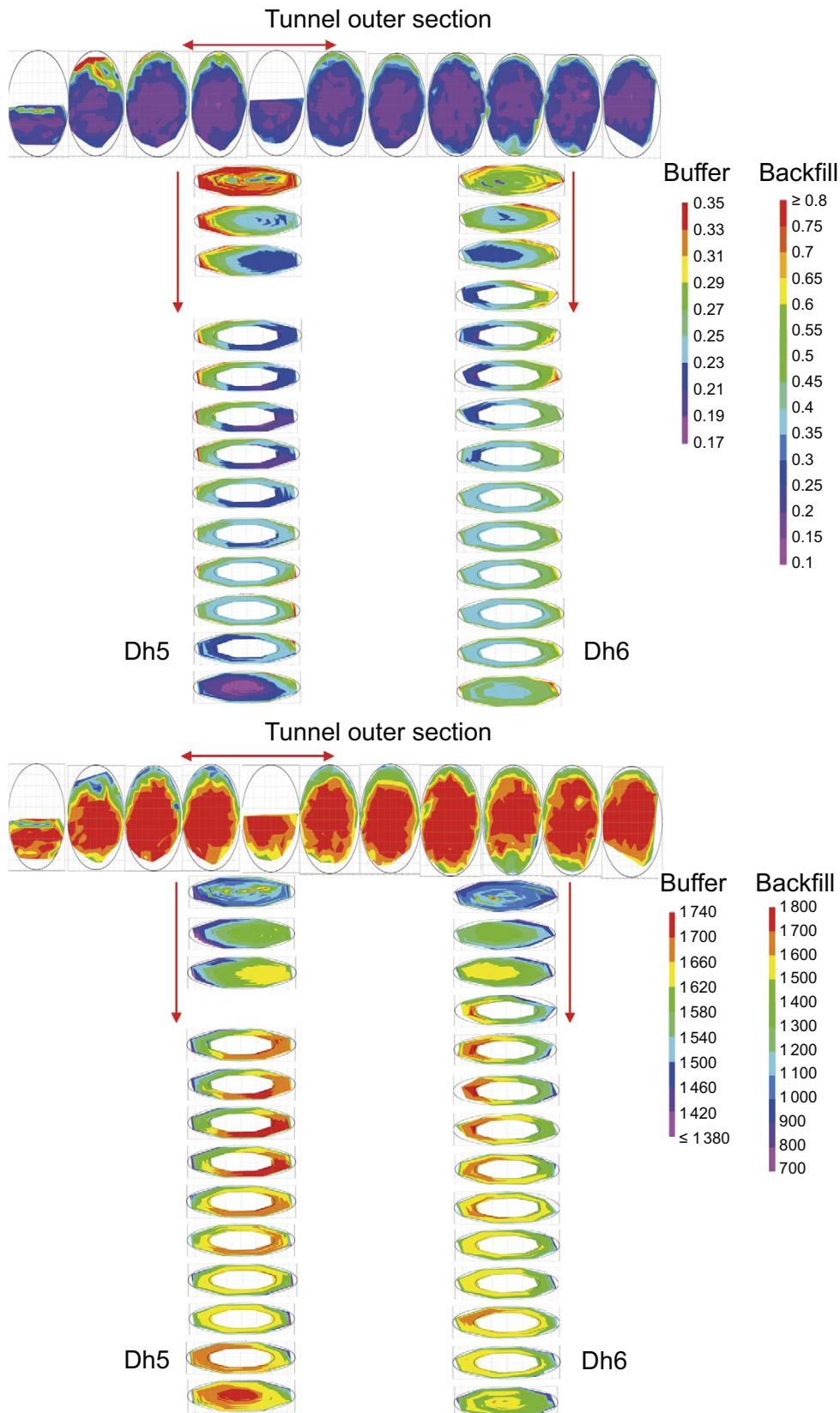


Figure 6-1. Compilation of water content (-, upper) and dry density (kg/m^3 , lower) distributions from the outer section of the Prototype repository (Johannesson 2014). Red arrows highlight areas with the highest water contents which indicate the occurrence of channel formation. The colours of the uppermost buffer blocks correspond to water contents (and dry densities) which were slightly higher (and lower) than those indicated by the scale.

6.3 Flow systems and phases

A general observation that can be made from the results from Subtask B is that at least three types of pore spaces, or *flow systems*, is needed in order to resemble the behavior of water uptake in pellets-filled slots: i) Micro pore flow. The permeability of this pore space is set by the bentonite material, and the main driving force for this is the suction gradient, and to some minor extent the boundary pressure; ii) Macro pore flow. The permeability of this pore space is set by pore geometry between the individual pellets, whereas the main driving force for this is the gravity and also to some minor extent the boundary pressure; and iii) Channel flow. The permeability of this set by the dimensions (the radius) of the channel which in turn is governed by the bentonite properties. The main driving force for this flow is the boundary pressure.

An attempt to describe the water uptake in a bentonite filling as sequence of four successive *phases* is shown in Figure 6-2. This illustrates a simple tunnel volume filled with bentonite blocks and pellets. The rock around the tunnel volume is intersected by a water bearing fracture which means that there is a localized water inflow with a specific rate. A schematic illustration of the evolution of the liquid pressure at the fracture, and the cumulative water uptake is shown in the lower panel. The water transport during the *first phase* is limited to water transport in the micro and the macro pore space and there may also be exchange from the macro to the micro pores. This phase is characterized by a low, but increasing, water pressure, and a constant rate of inflow to the tunnel volume. During the *second phase*, a successive formation of channel segments starts to take place. Due to the gravity, these channels tend sooner or later to move upwards and follow the tunnel ceiling. This phase is also characterized by a fairly constant inflow rate and quite low water pressure, and the pressure build-up is cut off due to the channel formation. During the *third phase*, the channel formation comes to a halt when the geometry of the tunnel volume limits any further extension of the channel. This means that the liquid pressure increases, at the same time as the inflow rate decreases. When this happens, it can be expected that previously unaffected dry parts of the bentonite in the vicinity of the channels is hydrated fairly quickly. This phase may also involve a compression of the part of the bentonite which still is unsaturated at this point. Finally, during the *fourth phase*, the water uptake is governed by a channel pressurized with hydrostatic pressure, which distributes the water uptake so that the entire tunnel eventually gets water saturated.

The relative importance of the different flow systems is likely to vary with time. This evolution can be assessed by analyzing the water uptake during each successive phase (see Table 6-1). During the *first phase*, there is by definition no channel flow, and both the micro and macro flow play dominant roles. For the micro pores this is however more a matter of water uptake rather than of actual transport. During the *second and the third phases* the channel flow plays the dominant role, whereas the micro and the macro flow are less important. During the *fourth phase*, which can be expected to have the longest duration, the micro flow will play a dominant role again. The channel flow will also be important, and will essentially distribute the boundary pressure along the length of the tunnel. However, it can also be expected that this channel will eventually heal due to the swelling of those part of the bentonite filling which is wetted lastly, and it is therefore uncertain how long this will contribute to the water uptake.

Needless to say, the development of channel flow system will greatly speed up the overall water uptake. This description implies that the gravity driven macro pore flow has a relatively marginal influence on the water uptake, although it is essential for describing the direction of the buildup of a channel. It can therefore be questioned how much effort should be put on the inclusion of this flow system in a water uptake model of this type of system. Moreover, if it could be shown that there will be a channel along the entire ceiling for instance under certain conditions, then this should imply that the overall water uptake calculation would be greatly simplified.

Table 6-1. Tentative summary of relative contribution of different flow systems during different flow phases.

| | Micro pore flow | Macro pore flow | Channel flow |
|------------------------|-----------------|-----------------|--------------|
| Micro/macro phase | Large | Large | |
| Piping phase | Small | Small | Large |
| Pressure buildup phase | Small | Small | Large |
| Main wetting phase | Large | | Large? |

- i. Micro/macro-phase
 - No channels
 - Low pressure
- ii. Piping phase
 - Channel extension
 - Threshold pressure
- iii. Pressure buildup phase
 - No further channelling
 - General pressure build-up
- iv. Main wetting phase
 - Channel healing
 - Hydrostatic pressure

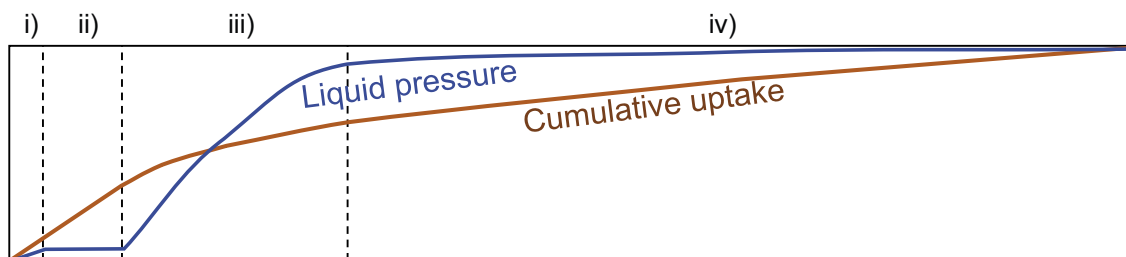
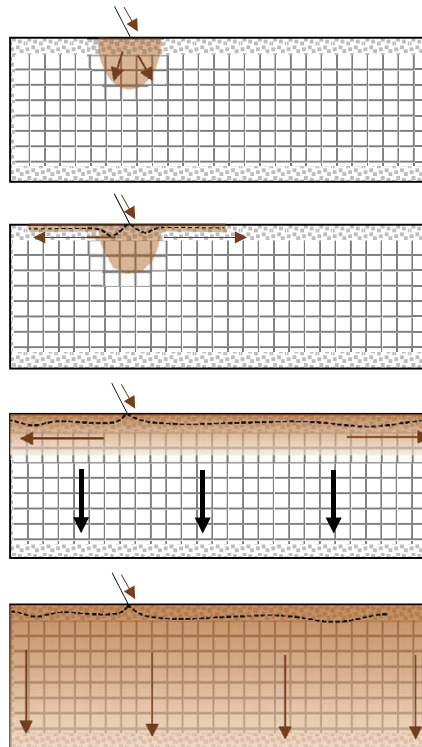


Figure 6-2. Schematic illustration of four flow phases (upper graphs) and of the evolution of the liquid pressure at the fracture and the cumulative water uptake (lower graph).

6.4 Hydromechanical interactions

Several of the contributions to subtask B showed that it is quite possible to include representations of sealing of macroscopic pore systems, and of the successive formation of permeable channel segments, without the inclusion of any mechanical processes. The flow systems and wetting phases outlined in the previous section could possibly also be reproduced as a purely hydraulic model. However, in order to be able to mimic the results from the Prototype repository, for example, it is clearly necessary to take the mechanical processes into account. One part of mechanical processes concerns the homogenization of the dry density differences built into the buffer and/or the backfill during the installation, and this has been addressed in several modeling tasks. A second, much less considered, aspect of the mechanical processes concerns hydromechanical response of buffer/backfill system, and how this is influenced by the hydraulic processes in the near-field rock.

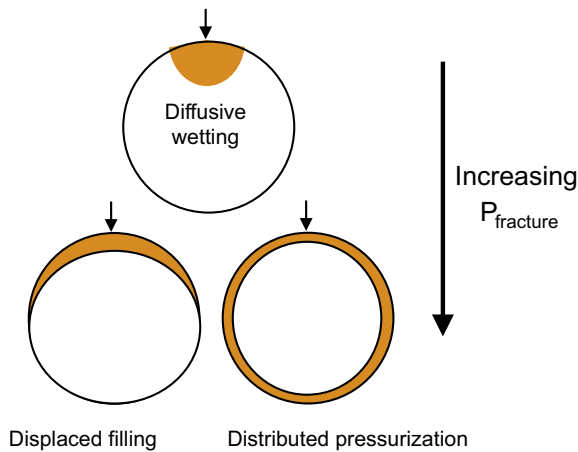
The water uptake in a bentonite filling is clearly influenced by the pore pressure at the water inlet (i.e. fracture) of the deposition hole/tunnel. Conditions with low pore pressure will result in a diffusion-like water uptake (Figure 6-3, upper), and an example of such wetting patterns conditions was observed in the BRIE-experiment (Fransson et al. 2017). In contrast, conditions with a high pore pressure can result in a channel formation along one side which in turn can lead to the displacement away from this channel, such as in the Prototype repository (Figure 6-1). An alternative wetting pattern could be a more distributed pressure distribution, which could either be a result of channel formation in the pellets filling, or perhaps via fractures/EDZ in the rock close to the tunnel (Figure 6-3, upper), and an example

of such wetting patterns conditions was observed in the Domplu-experiment (Åkesson et al. 2019). The extent of channel formation and displacements, for a given inlet pore pressure, should be influenced by the hydromechanical response and thus the compressibility of the buffer/backfill-system.

The pore pressure at the water inlet of the deposition hole/tunnel is influenced by the hydraulic processes in the near-field rock. More specifically, the relation between the pore pressure at the inlet and the flow rate should be influenced by the transmissivity of the fracture, and the near-field pore pressure in the rock (Figure 6-3, lower). For example, for an open tunnel, the inlet pore pressure is zero while the inflow rate has a certain value. If the transmissivity is assumed to be constant, two things can happen: i) the flow resistance downstream the fracture may increase which leads to a reduction in the flow rate and an increase in the inlet pressure; or ii) the near-field pore pressure in the nearby rock, may increase which leads to an increasing flow rate. The actual relation between the inlet pressure and the flow rate will be determined by in which order these changes will take place.

These influences should therefore be represented in a model of the wetting of the buffer/backfill-system in order to predict the water uptake as accurately as possible.

Influence from buffer/backfill:



Influence from rock:

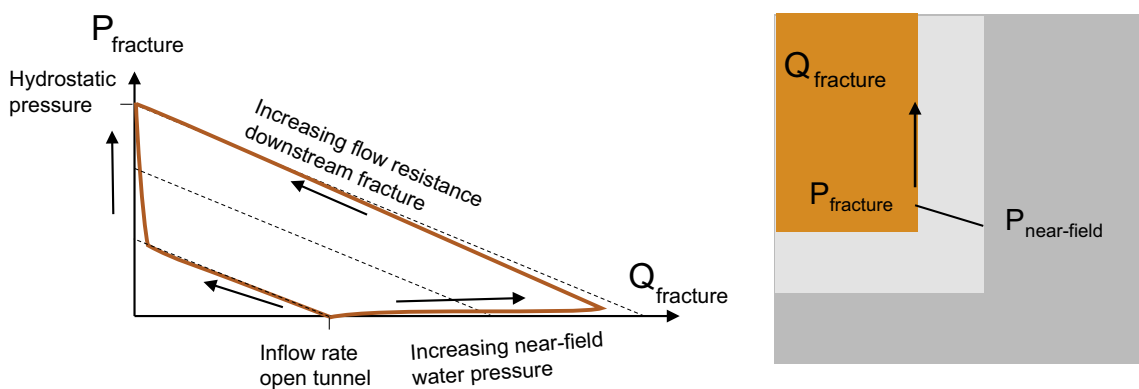


Figure 6-3. Tentative identification of different mechanism influencing the wetting pattern. Hydromechanical response from buffer/backfill leading to localized or more distributed wetting (upper), hydraulic boundary conditions defined by the rock and different pressure-flow rate responses determined by the fracture transmissivity and the near-field water pressure (lower).

7 Concluding remarks

The modelling work presented within subtask A and C has shown that the established thermo-hydraulic constitutive relations: i) water retention curves; ii) the Darcy's law for unsaturated liquid transport; and iii) vapor diffusion, can essentially describe the processes in both the investigated test types.

From the modelling work presented in subtask B, the following observations can be made:

- i. A *reduction of the permeability* for macroscopic porewater in a pellet medium, following from the *absorption of this porewater*, appears to be a suitable approach for simulating the increasing water pressure at the water inlet.
- ii. The transport of macroscopic porewater through a high permeability pellets medium, appears to be *numerically more stable*, if the description of the pressure-water content relation (e.g. the water retention curve) is *not based on capillary/osmotic action* and that the liquid pressure exceeds the gas pressure.
- iii. The *formation of channels* can be implemented through modification of the *permeability field or the geometry*. Such modifications rely on the available options provided by the code.
- iv. The flow of macroscopic porewater seems to govern the *direction of channel formation*, but appears to provide only a *limited contribution* to the overall water uptake in a large-scale buffer/backfill system.

From these observations it seems to be important to be able to include a representation of channel flow in order to resemble the wetting behaviour of large-scale deposition holes and tunnels. Both the successive extension and the healing/closing of a channel system may play a crucial role for making accurate predictions.

A relatively simple form of representing a channel system may be to include pre-defined channel materials which pragmatically could be localized from an intersecting fracture and upwards, as well as along the tunnel ceilings. The main difference between such a material and a normal pellets-filling would be its high permeability, which possibly could be activated or disabled during certain conditions. Such an approach could essentially be implemented in a thermo-hydraulic framework.

In contrast, a fully-coupled THM framework would be required in order to include the hydro-mechanical responses of the buffer/backfills, with displacements of blocks and the formation of pressurized zones with low dry density. The latter effect would constitute a more physical representation of a channel system. Still, some form of pre-determined localization (e.g. from fracture to tunnel end) would probably be needed, if the challenges associated with macroscopic porewater are to be avoided.

References

SKB's (Svensk Kärnbränslehantering AB) publications can be found at www.skb.com/publications.

Aro T, Heikkilä A, Rönnblad S, Tanttari J, 2019. Bentonite pellets flow resistance. Elomatic Document 25608-001/ Posiva public memorandum POS-029785, Posiva Oy, Finland.

Börgesson L, Sandén T, Dueck A, Andersson L, Jensen V, Nilsson U, Olsson S, Åkesson M, Kristensson O, Svensson S, 2015. Consequences of water inflow and early water uptake in deposition holes, EVA project. SKB TR-14-22, Svensk Kärnbränslehantering AB.

Eriksson P, 2019. Development of thermo-hydraulic model for pellet fillings. SKB P-19-12, Svensk Kärnbränslehantering AB.

Eriksson P, 2020. Effects of water inflow to deposition hole during the installation phase. SKB R-20-07, Svensk Kärnbränslehantering AB.

Fransson Å, Åkesson M, Andersson L, 2017. Bentonite Rock Interaction Experiment. Characterisation of rock and installation, hydration and dismantling of bentonite parcels. SKB R-14-11, Svensk Kärnbränslehantering AB.

Johannesson L-E, 2014. Prototype Repository. Measurements of water content and density of the excavated buffer material from deposition hole 5 and 6 and the backfill in the outer section of the Prototype Repository. SKB P-13-14, Svensk Kärnbränslehantering AB.

Kristensson O, Malmberg D, Åkesson M, 2022. EBS TF – THM modelling. Water transport in pellets-filled slots. Modelling of test case B. SKB P-22-20, Svensk Kärnbränslehantering AB.

Martikainen J, Laurila T, Leino T, 2017. Backfill pellets wetting behavior tests. Posiva public memorandum POS-029773, Posiva Oy, Finland.

Wu J, Jackson C P, Holton D, 2021. Modelling the bentonite pellet experiments. RWM008754, Jacobs Clean Energy Limited, UK.

Åkesson M, 2020. EBS TF – THM modelling. Water transport in pellets-filled slots – evaluation of model contributions. SKB P-20-18, Svensk Kärnbränslehantering AB.

Åkesson M, Sandén T, Goudarzi R, Malmberg D, 2019. Full-scale test of the Dome Plug for KBS-3V deposition tunnels. Monitoring, function tests and analysis of bentonite components. SKB P-18-15, Svensk Kärnbränslehantering AB.

Task description

Modelling of water transport in pellet filled slots – modelling task for TF EBS phase 3

Addition of Subtask B. Constant water inflow rate from point inflow.

Results are from work done by Jari Martikainen, Teemu Laurila and Teemu Leino, Saanio & Riekkola Oy.

Editing of results for TF EBS phase 3 by Mika Niskanen, Posiva Oy.

The complete report "Backfill pellets wetting behavior tests" is also available from the Task Force member pages.

Modelling task description

- Use similar bucket/box setup geometry as given in pages 3 and 4.
- Simulate wetting pattern and water content evolution, optionally also upheave of pellet surface.
- 1st phase: symmetric model, wetting evolution upwards/downwards/sideways in bucket and upwards/sideways in box.
- 2nd phase: randomize porosity/dry density distribution of pellets/use single pellets and packing, wetting evolution upwards/downwards/sideways in bucket and upwards/sideways in box.

Key question: What kind of model is needed for capturing wetting caused by flow channels? Can it be implemented in THM codes, possibly in simplified form?

Bentonite pellets description

Extruded 6 mm rod-pellets (Cebogel QSE). The Cebogel QSE pellets were manufactured by Cebo Holland from Sodium-activated Milos bentonite. The pellets were pre-sieved at factory and used as received. Figure A-1 shows typical Cebogel QSE pellets.

Material properties

Montmorillonite content: ~80 %.

Grain density: ~2.795 g/cm³.

Water content: ~21 %.



Figure A-1. Extruded 6 mm rod-shaped Cebogel QSE pellets as received.

Individual pellet properties

Bulk density: $1.95 \text{ g/cm}^3 - 2.04 \text{ g/cm}^3$ (mean 2.00 g/cm^3 , stdev 0.02 g/cm^3).

Length: 9.7 mm to 26.7 mm (mean 17.4 mm, stdev 4.1 mm).

Diameter: 5.8 mm to 6.5 mm (mean 6.2 mm, stdev 0.2 mm).

Installed pellet-mass properties

Are given later in subtask B test description.

Data for subtask B – 3D-tests with constant water inflow rate from point inflow

Test layout

In first test series “borderless” wetting conditions were employed with the inflow point located in the middle of the pellet filling. The inflow rate and pellet-filled volume ratio were selected so that wetting would principally occur before the effect of confining walls or bottom would need to be taken into account. The goal was to achieve 3D wetting pattern without wall and floor contact and to determine the maximum downwards wetting length prior to upwards migration. The test setup was 200 L bucket as shown in Figure A-2.

In the second series floor wetting tests were done wherein the inflow point was located in the middle of the bottom of the pellet filling (underneath pellet material). The inflow rate and pellet-filled volume ratio were selected so that wetting would occur without the effect of confining walls. The goal in the floor wetting test series was to achieve 3D wetting pattern without wall contact and to determine the wetting length along the floor before wetting goes upwards, piping channel forms to the surface and wetting happens along the pellet surface. By using the inflow point location on the floor (the lowest point in the backfill tunnel), the maximum wetting length along the floor before wetting goes upwards can be determined. The test setup was 571 L box as shown in Figures A-3 and A-4. Tests were done with and without added surface load. It was observed in earlier floor layer tests that additional surface load promotes upwards wetting so this was tested again.

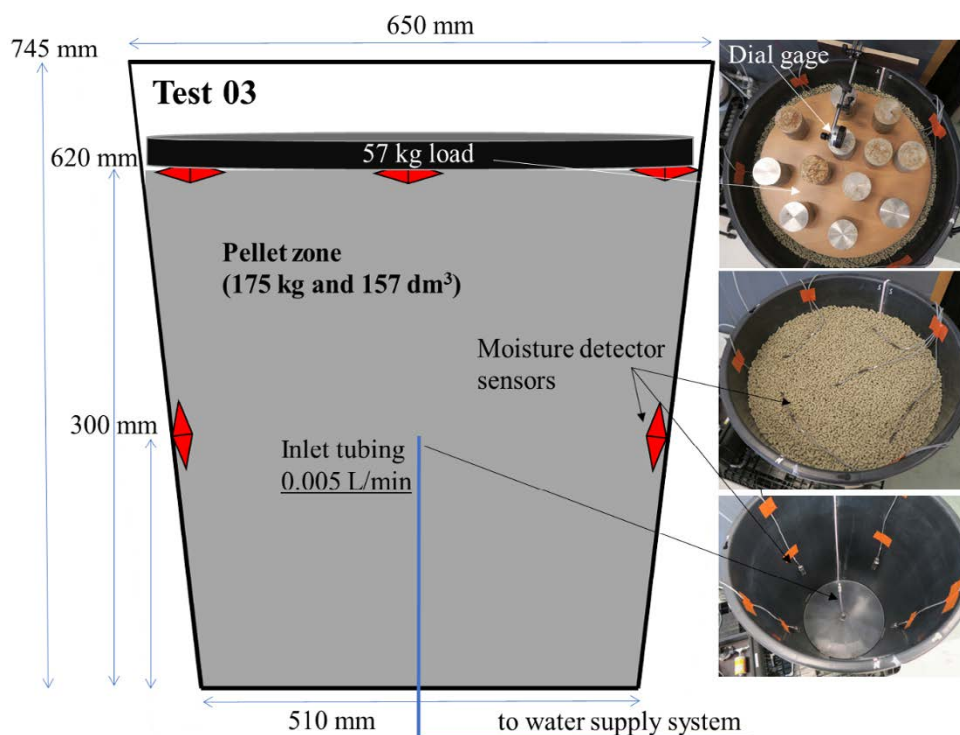


Figure A-2. Cross-section schematic illustration of the test system (left) with initial pellet volume dimensions, water inlet position and location of moisture detector sensors and photographic images (right) showing test setup in the 3D wetting test 03. A surface load (57 kg) on the top of the pellet-filling was used in test 03. A dial gage measured vertical displacement at the top of the surface load. The inlet tubing was led through the bottom at the center of the bucket.

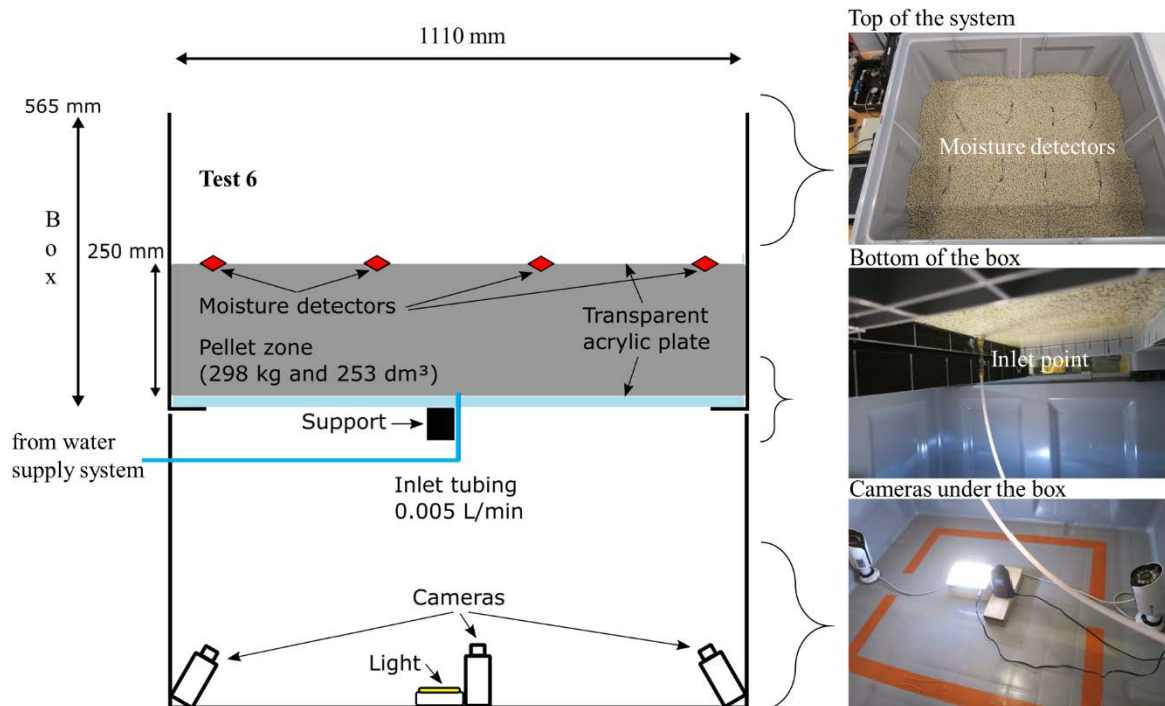


Figure A-3. Cross-section schematic illustration of the test system (left) showing test setup, initial pellet volume dimensions, water inlet position and location of moisture detector sensors and photographic images (right) of floor wetting test 06.

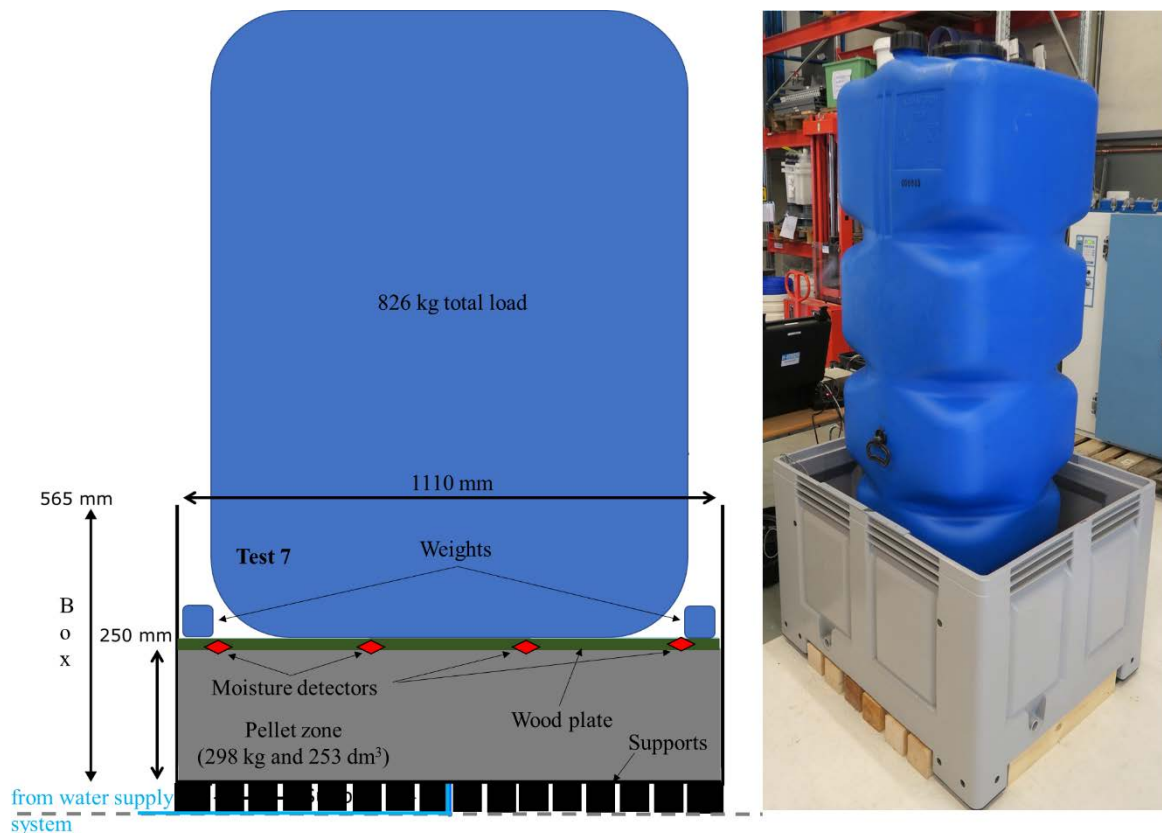


Figure A-4. Cross-section schematic illustration of the test system (left) showing test setup, initial pellet volume dimensions, water inlet position and location of moisture detector sensors and photographic images (right) of floor wetting test 07. A surface load (826 kg) on the top of the pellet-filling was used in the test.

Table A-1 below has list of initial conditions for tests 3, 6 and 7.

Table A-1. Initial conditions for borderless wetting tests. Test 03 is a 3D wetting test and tests 06 and 07 are floor wetting tests.

| | Test 03 | Test 06 | Test 07 |
|--|----------------------|-------------------|---------------------|
| Pellet type | Cebogel QSE | Cebogel QSE | Cebogel QSE |
| Water content [%] | 21.3 | 20.83 | 21.04 |
| Test system | 200 L bucket | 571 L box | 571 L box |
| Test system dimensions, height x width x length ¹ [mm] | 745 x 650 (diameter) | 565 x 910 x 1 110 | 565 x 910 x 1 110 |
| Measured pellet filling height after installation ¹ [mm] | 620 | 250 | 250 |
| Pellet filling volume estimation [dm ³] | 157 | 253 | 253 |
| Void and pore volume sum estimation at pellet filling [dm ³] | 106 | 164 | 164 |
| Weighed bulk mass ² [kg] | 175 | 298 | 298 |
| Calculated dry mass [kg] | 144 | 246 | 246 |
| Calculated average dry density [kg/m ³] | 917 | 975 | 975 |
| Calculated degree of saturation | 29.1 % | 31.5 % | 31.4 % |
| Initial Conditions | Test 03 | Test 06 | Test 07 |
| Saturating solution ³ [g/L] | 10 | 10 | 10 |
| Inflow rate [L/min] (target 0.005 L/min) | 0.0045 | 0.006 | 0.0065 |
| Added surface load | 57 kg (1.7 kPa) | not used | 826 kg (8.0 kPa) |

¹ Measurement precision is millimeter.

² Measurement precision is 0.01 kilograms.

³ A reference, groundwater simulant (total dissolved solids = 10 g/L, Ca²⁺/Na⁺ mass ratio = 1:2) was used in all of the tests.

Test results

Test 03

The inflow rate and inflow pressure are given in Figure A-5. After 72 hours (corresponding to the inflow volume of 21.6 L, enough to fill 20.4 % of the initial, available void volume), water was observed at the top of the pellet filling and the pump was stopped and setup was dismantled. As can be seen in Figure A-6, water reached the top of the pellet surface at the center of the bucket. Presumably, the water reached the top of the pellet filling earlier than when the pump was stopped since the size of the wetted area was approximately 15 × 20 cm at the end of the test.

Swelling of the pellet filling volume was observed during test 03. Vertical displacement of the pellet filling was measured from one point on the top of the added surface load over the course of the test, see Figure A-7.

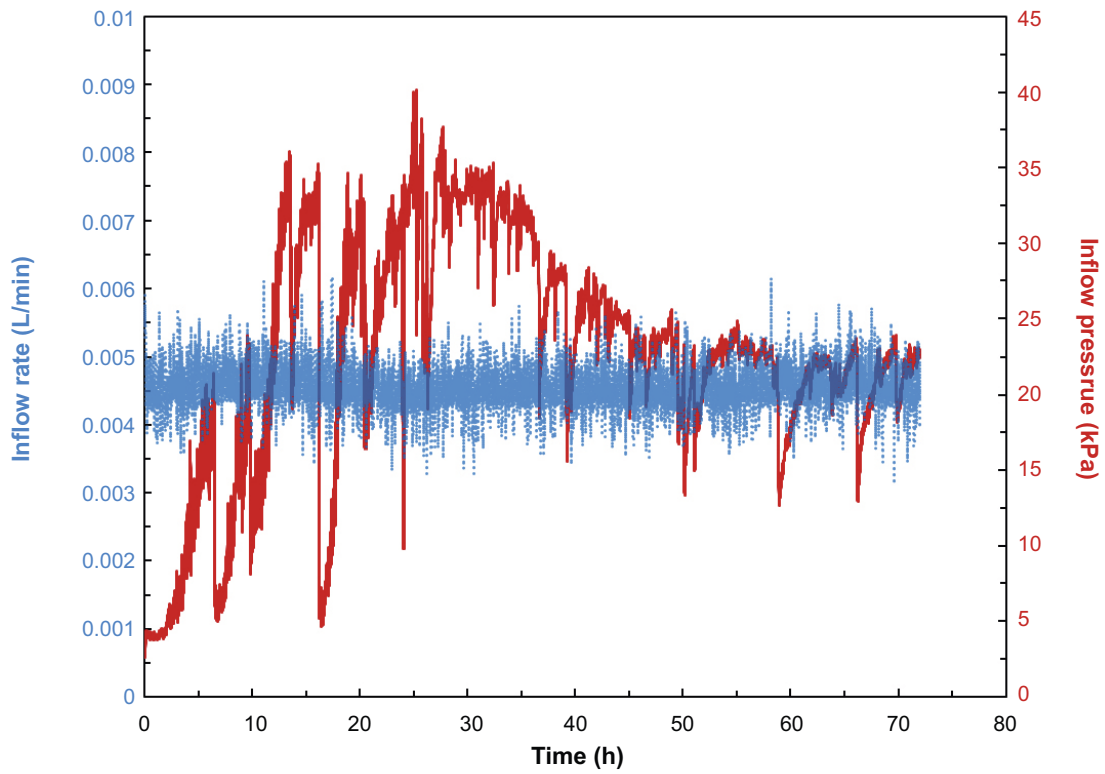


Figure A-5. Inflow rate (blue) and inflow pressure (red) measured over the course of 3D wetting test 03. Inflow rate data is plotted as a moving average (each point is average value over 60 seconds, corresponding six measurements).

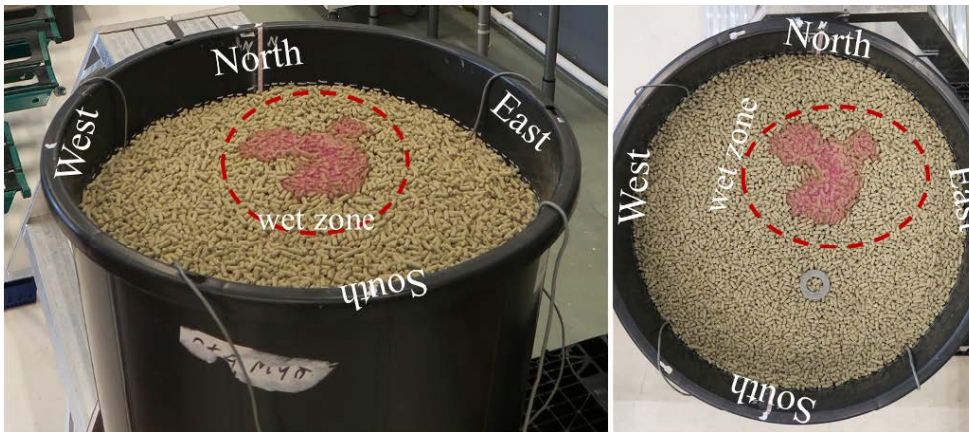


Figure A-6. Photographic images of test 03 at the end of the test when the water reached the top of the pellet surface at the center of the bucket (red color is due to added dye in the pumped water).

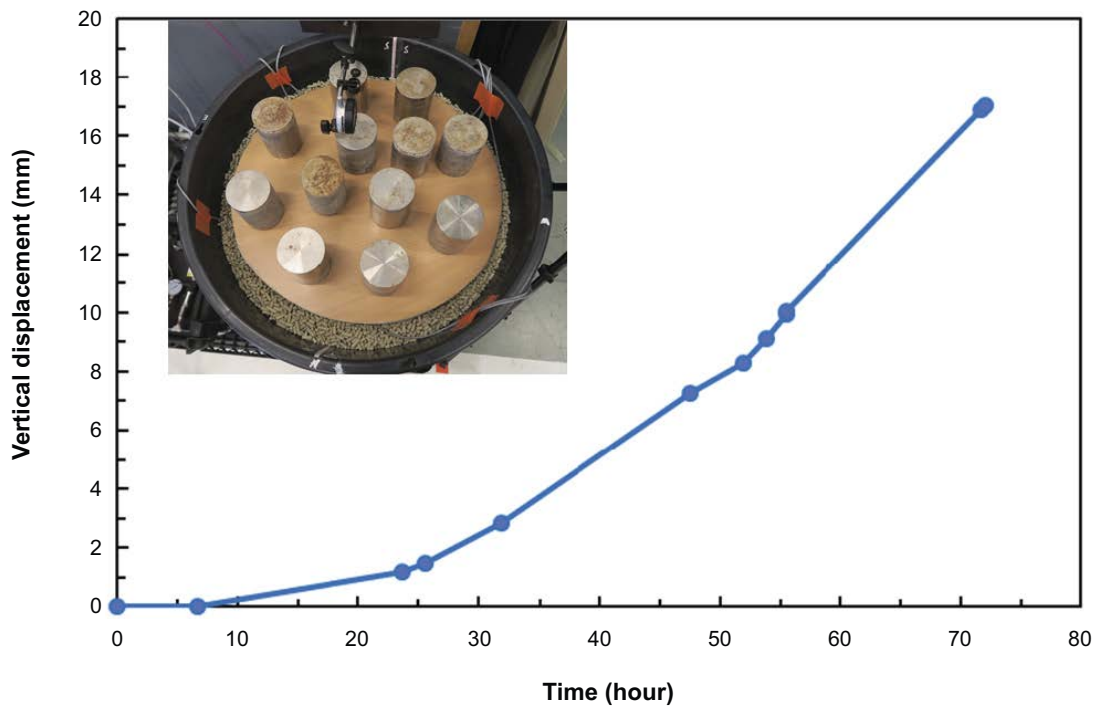


Figure A-7. Vertical displacement as a function of time over the course of test 03. The measurement was performed by dial gauge from one point on the top of the added surface load over the course of the test (see photographic image).

The pumped water into the test system was dyed with blue and red colors over specific time spans in test 03 (see Table A-2) to get a better understanding of water infiltration behavior during the test. The dyed areas revealed during the dismantling are shown in Figure A-8, qualitative wetting patterns in Figure A-9 and constructed 3D wetting maps in Figure A-10. Moreover, samples were collected for water content analysis. The results are shown in Figure A-11.

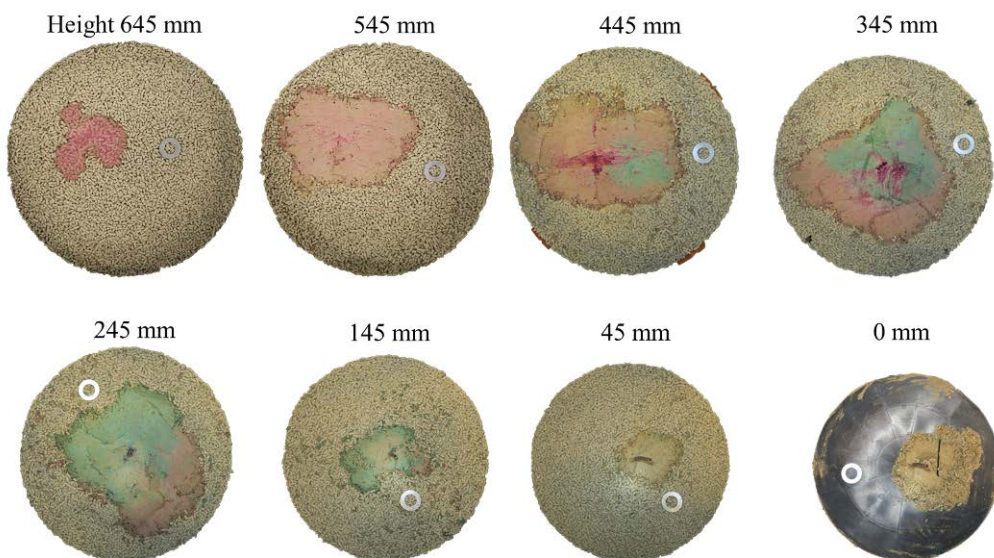


Figure A-8. Layer surfaces of test 03 over the height of the pellet filling at the end of the test (after 72.0 hours). Note, the inlet tubing was located at a height of 300 mm in the middle of the pellet filling (not seen in images).

Table A-2. Times when pumped water into the test system was dyed with each color.

| Added color to pumped water | Time between | Duration |
|---|--------------|----------|
| No added dye (shown in black in Figures A-9 and A-11) | 0–6.6 h | 6.6 h |
| Blue | 6.6–24.0 h | 17.4 h |
| Red | 24.0–72.0 h | 48.0 h |

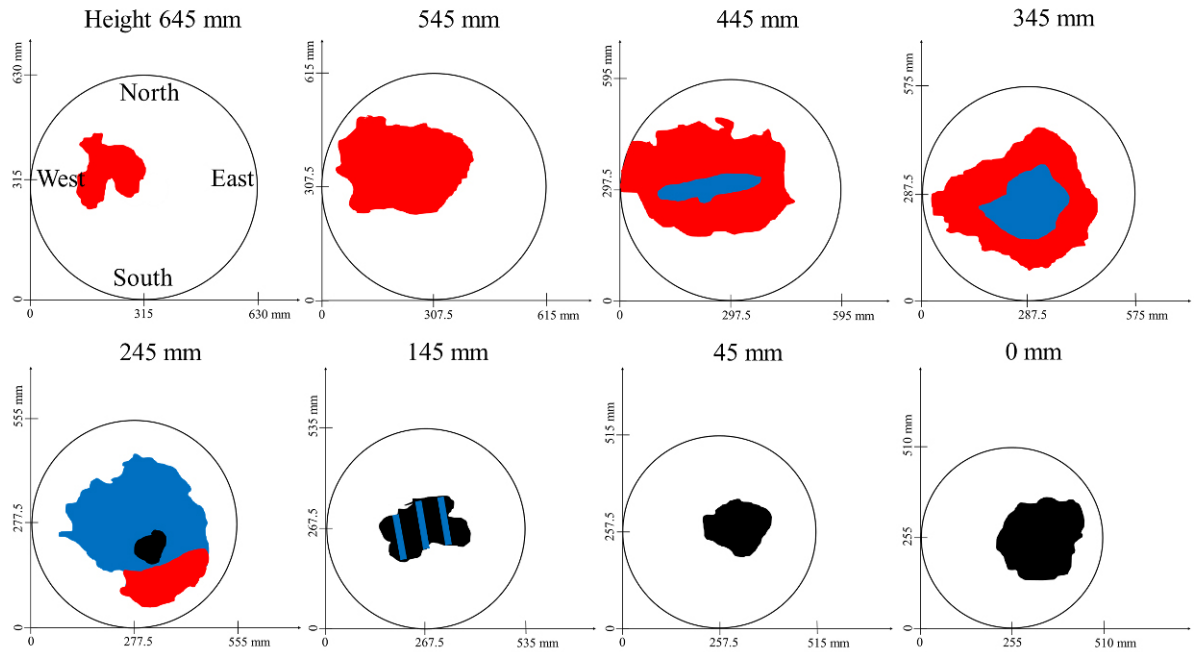


Figure A-9. Qualitative wetting pattern threshold (colors correspond to the dyes over the specific time spans according to Table 3-2 and white areas to visually dry pellet zones) images for test 03 over the pellet filling height at the end of the test (after 72.0 hours). At a height of 145 mm the wetted area was mixture of both the initial undyed solution (black color in images) and after addition of blue dye. The inlet tubing was located at a height of 300 mm in the middle of the pellet filling (marked with light blue dot).

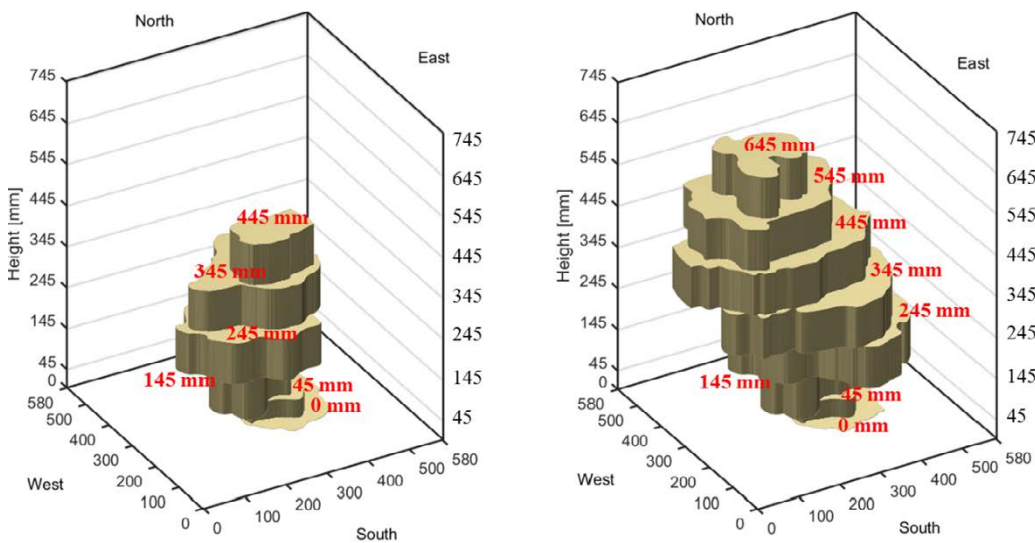


Figure A-10. 3D qualitative wetting pattern images for test 03 over the pellet filling volume after 24.0 hours (left) and at the end of the test (right). The height of surface layers in 3D wetting pattern image is indicated with red color. Note, sharp edges between layers are artefacts due to 3D image was constructed from 2D images (see Martikainen et al. 2017) by image analysis program and the diameter of the bucket is normalized to 580 mm over the height of the pellet filling.

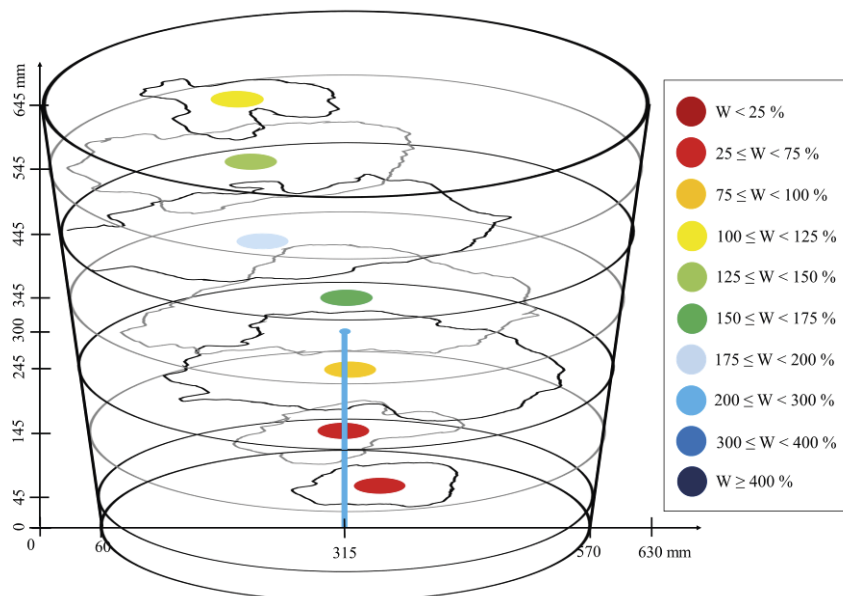
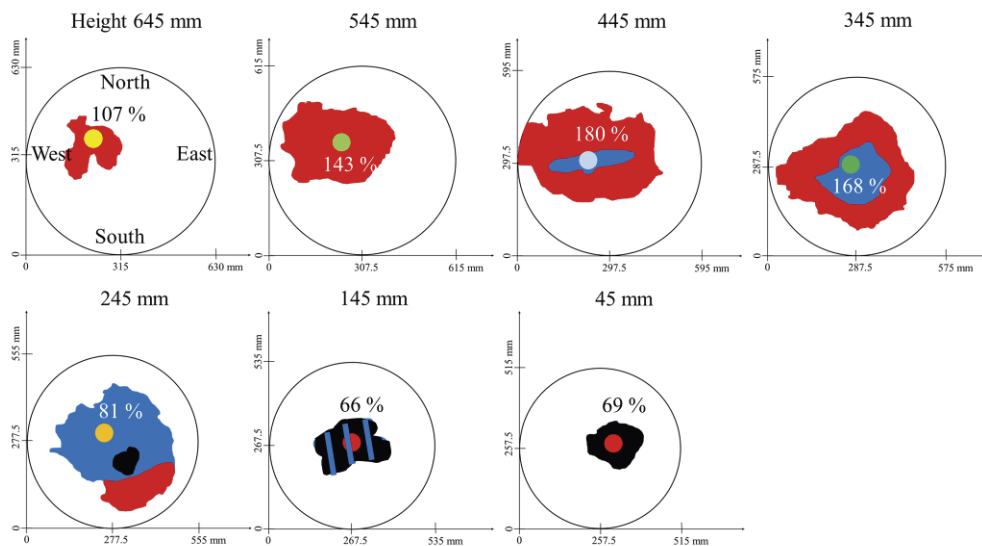


Figure A-II. Sample water contents over the height of the pellet-filled volume at the end of test 03 (72.0 hours) in 2D (top) and 3D images (bottom). Circles indicate the sampling location at each height and water content value is indicated by color (see table in the bottom image). Black and gray outlines represent wetting patterns at each height in bottom image. Note, the inlet port located at a height of 300 mm and tube in the middle of the pellet filling are marked in light blue line in the bottom image.

Test 06

The measured inflow rate and resistance to inflow (inflow pressure) for test 06 are shown in Figure A-12. The wetting did not reach the top of the pellet surface (Figure A-13.) The pump was stopped after 40 hours and total inflow to the system was 12 L (enough to fill 7.3 % of initial available void volume).

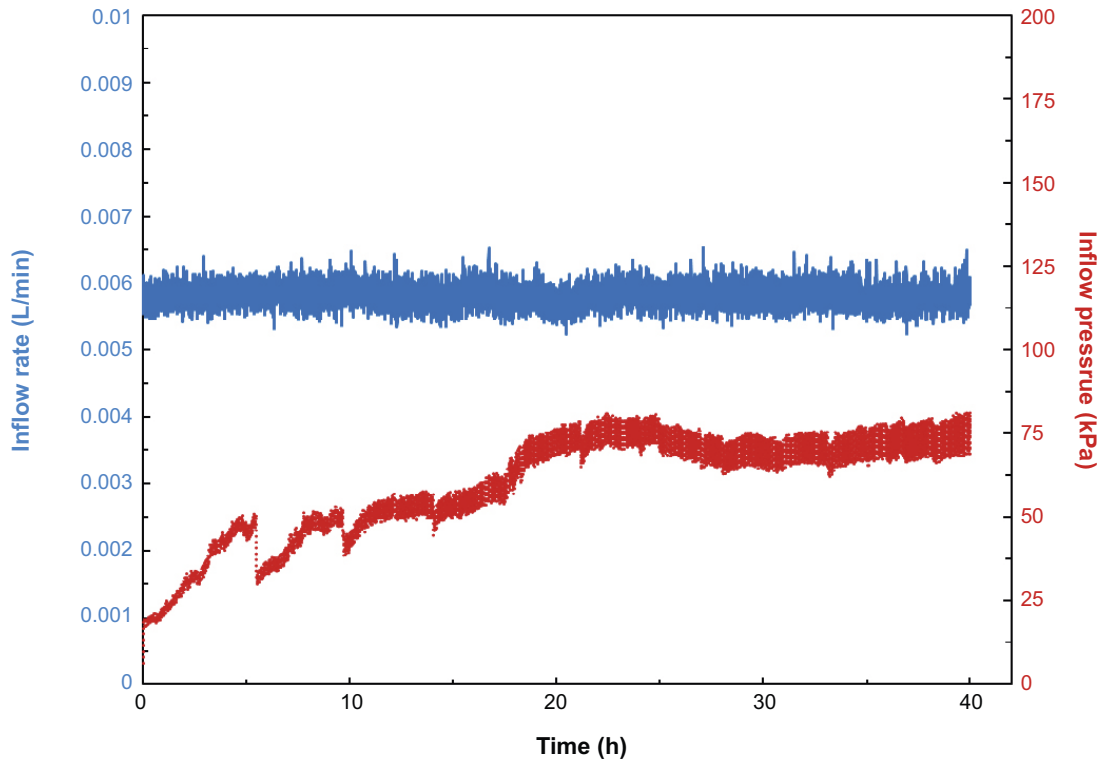


Figure A-12. Inflow rate (blue) and inflow pressure (red) measured over the course of floor wetting test 06. The inflow pressure line is a moving average of 5 measurements (each point corresponding to a 100 seconds period).



Figure A-13. Photographic images of test 06 at the end of the test after 40.0 hours. Wetting did not reach the top of the pellet surface during the test.

Local swelling of the pellet-filled volume was observed in test 06. Vertical displacement of the pellet filling was measured locally from several surface locations (see Figure A-14). Similarly, to the previous tests, the pumped water into the test system was dyed with blue and red colors over specific time spans (see Table A-3). The dyed areas revealed during the dismantling are shown in Figures A-15 and A-16, qualitative wetting patterns in Figure A-17 and constructed 3D wetting maps in Figure A-18. Moreover, samples were collected for water content analysis. The results are shown in Figure A-19.

Table A-3. Times when pumped water into the test system was dyed with each color.

| Added color to pumped water | Time between | Duration |
|---|--------------|----------|
| Blue | 0–17.2 h | 17.2 h |
| Red | 17.2–23.9 h | 6.7 h |
| No added dye (shown in gray in Figure A-17 and Figure A-19) | 23.9–40.0 h | 16.1 h |

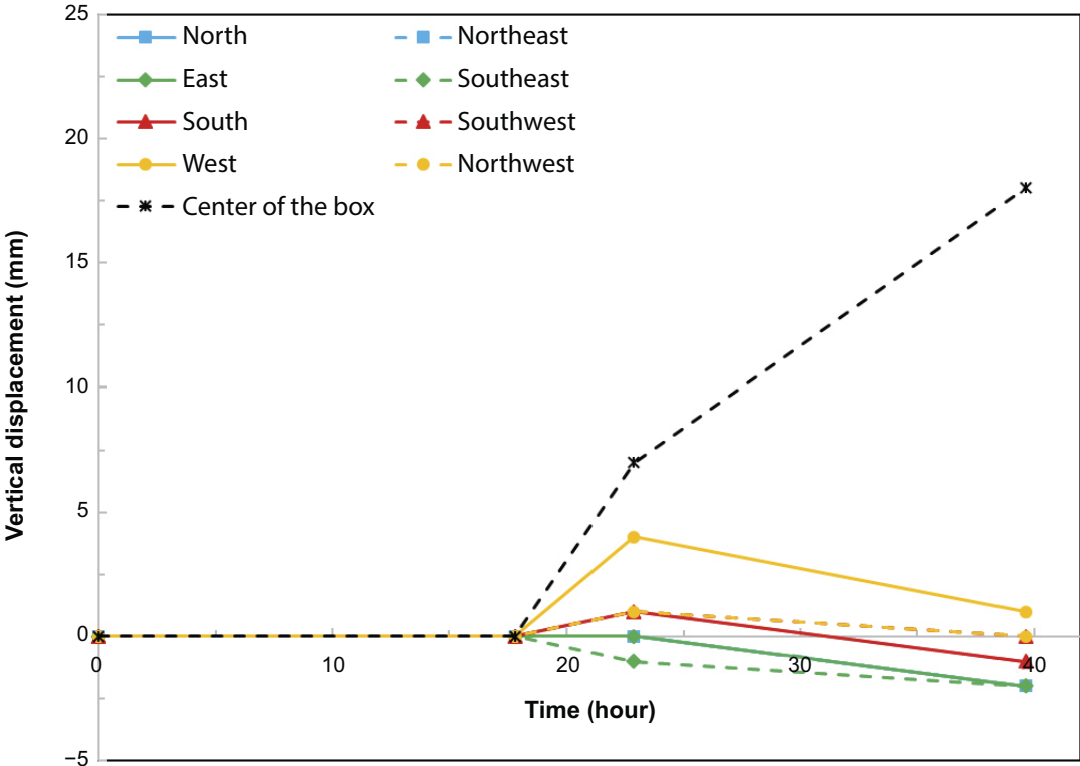


Figure A-14. Vertical displacement of the pellet filling as a function of time over the course of test 06. Vertical displacement was measured on the top of the pellet filling surface.

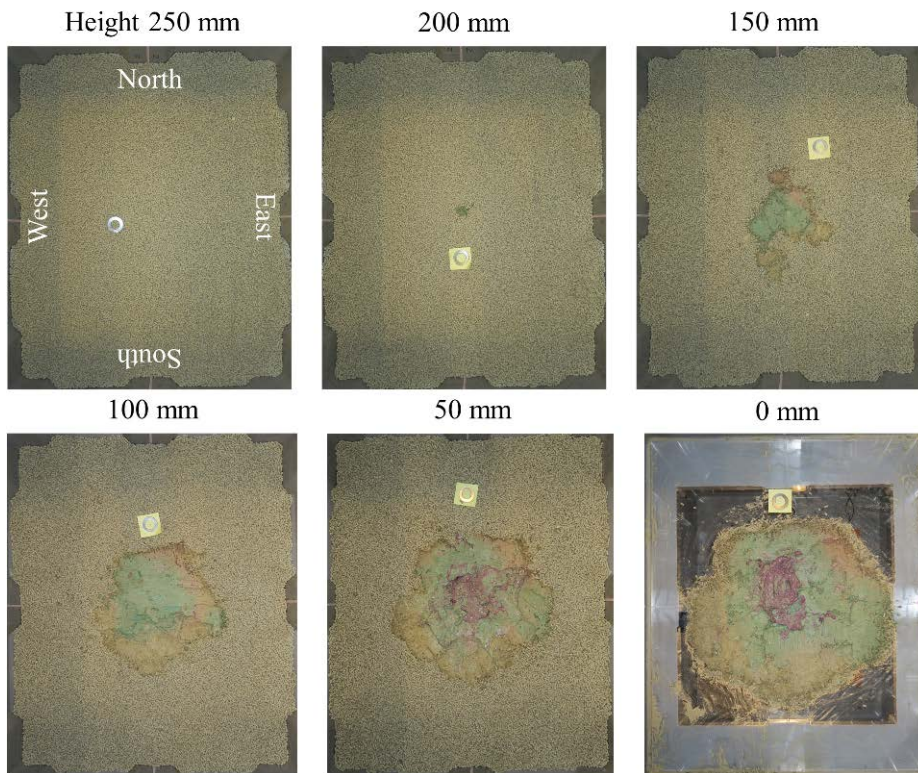


Figure A-15. Appearance of test 06 over each sampling height of the pellet filling at the end of the test (after 40.0 hours). Note, the inlet tubing was located in the middle of the bottom (not seen in 0 mm image).

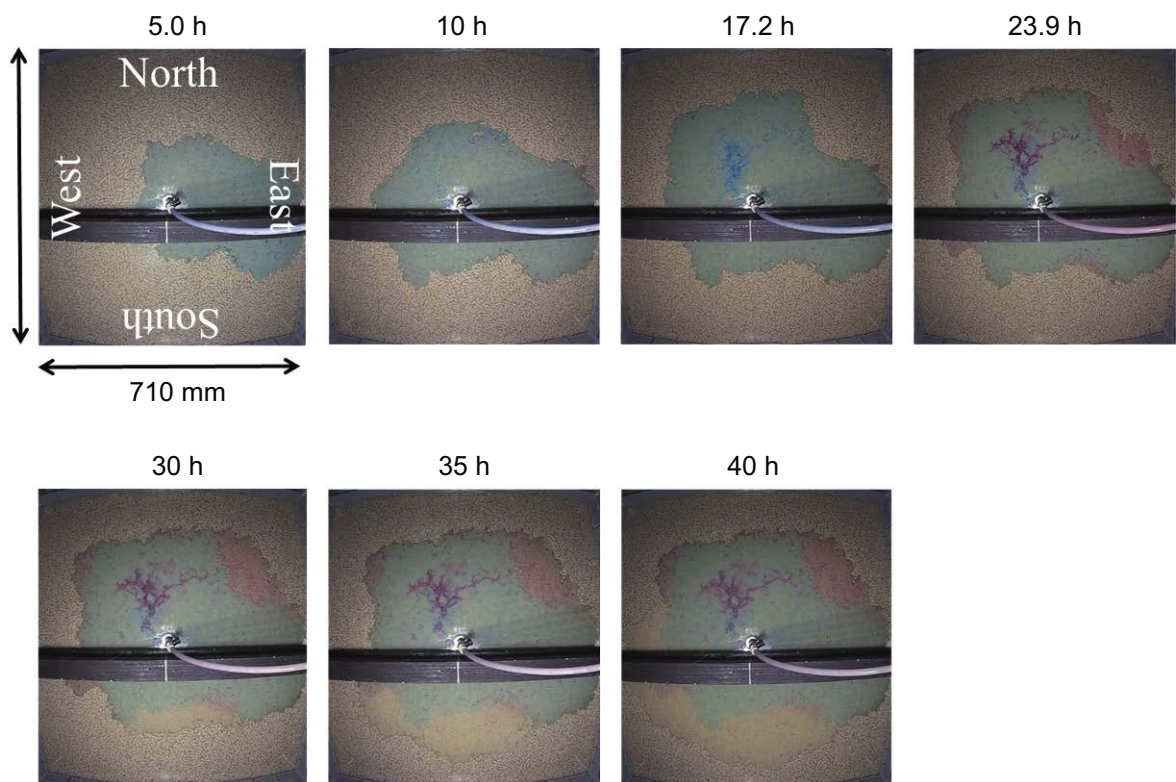


Figure A-16. Appearances of the bottom of test 06 as a function of the time. Note, the recorded area does not encompass the entire pellet filling area (1 110 x 910 mm).

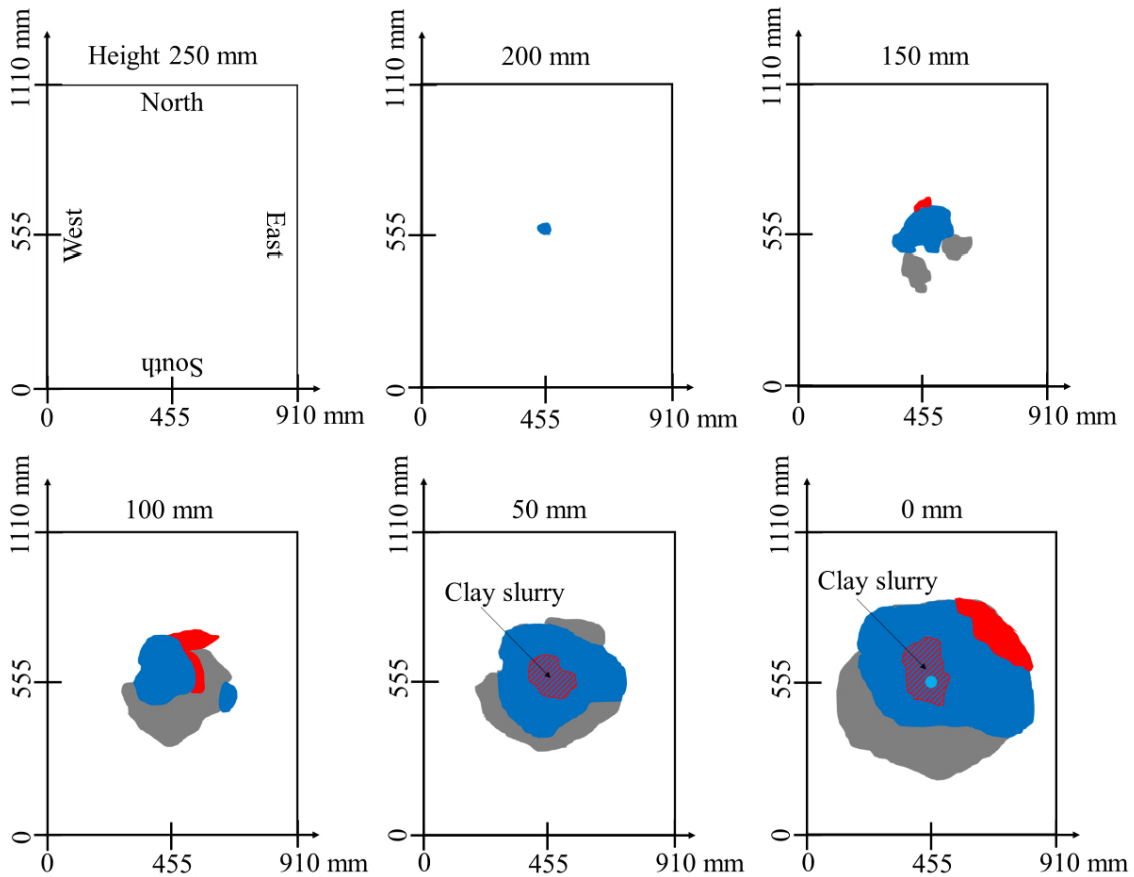


Figure A-17. Qualitative wetting pattern threshold (colors correspond to the dyes over the specific time spans according to Table 4-3 and white areas to visually dry pellet zones) images for test 06 over the pellet filling height at the end of the test (after 40.0 hours). At heights of 50 and 0 mm, the blue color with red stripes represent a mixture of both colors. The inlet port was located in the middle of the bottom of the box (marked with light blue dot).

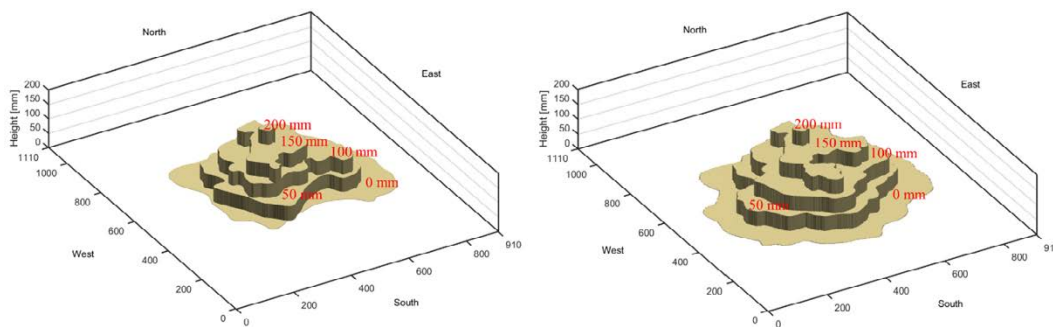


Figure A-18. 3D qualitative wetting pattern images for test 06 over the pellet filling volume after 23.9 hours (left) and at the end of the test (right). The height of surface layers in 3D wetting pattern image is indicated with red color. Note, sharp edges between layers are artefacts due to 3D image was constructed from 2D images (see Martikainen et al. 2017) by image analysis program.

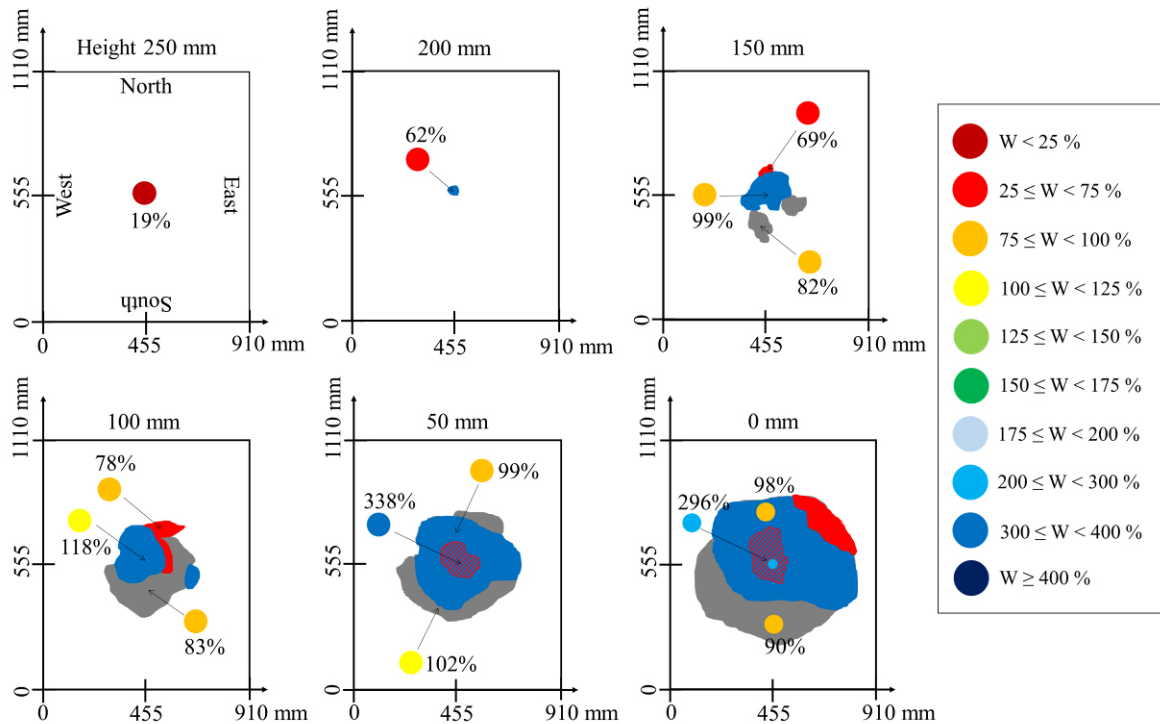


Figure A-19. Sample water contents over the height of the pellet-filled volume at the end of test 06 (40.0 hours). Circles indicate the sampling location at each height and water content value is indicated with colors (see table in the right). Note, the inlet port was in the bottom of the box (not seen in image).

Test 07

The measured inflow rate and resistance to inflow (inflow pressure) for test 07 are shown in Figure A-20. The wetting reached the top of the pellet surface (Figure A-21). The pump was stopped after 64.1 hours and total inflow to the system was 19.2 L (enough to fill 11.7 % of initial available void volume).

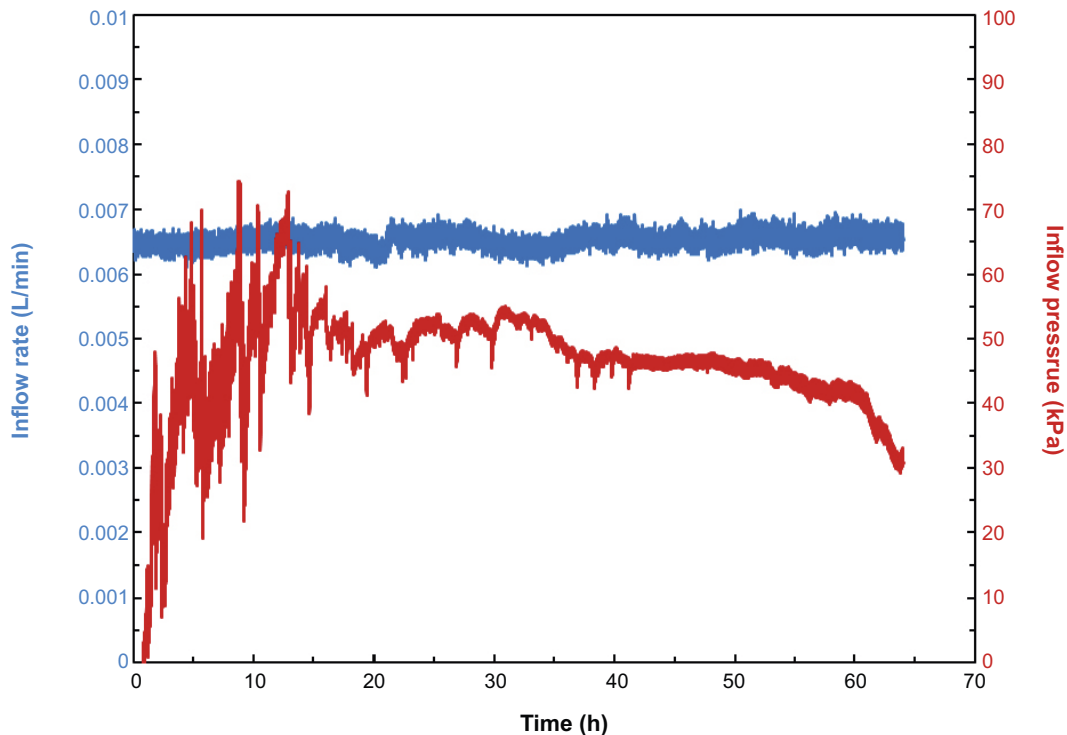


Figure A-20. Inflow rate (blue) and inflow pressure (red) measured over the course of floor wetting test 07.

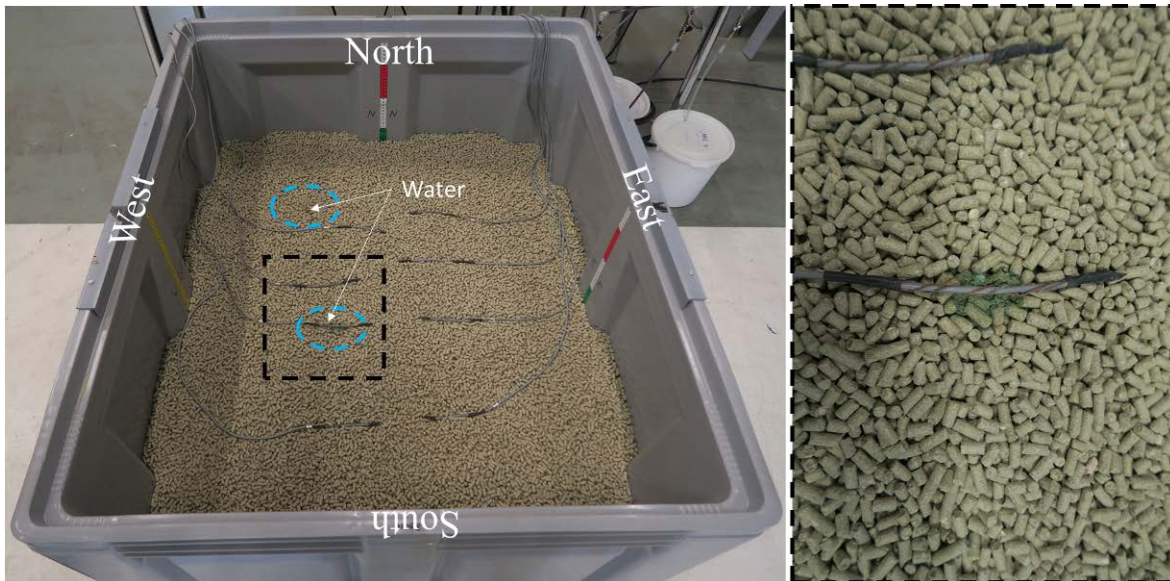


Figure A-21. Top view (left) and close-up photographic image (showing surface wetting) of test 07 at the end of the test (after 64.1 hours).

Local swelling of the pellet-filled volume was observed in test 07. Vertical displacement of the pellet filling was measured locally from several surface locations (see Figure A-22). Similarly, to the previous tests, the pumped water into the test system was dyed with blue and red colors over specific time spans (see Table A-4). The dyed areas revealed during the dismantling are shown in Figure A-23, qualitative wetting patterns in Figure A-24 and constructed 3D wetting maps in Figure A-25. Moreover, samples were collected for water content analysis. The results are shown in Figure A-26.

Table A-4. Times when pumped water into the test system was dyed with each color.

| Added color to pumped water | Time between | Duration |
|---|--------------|----------|
| Blue | 0–24.2 h | 24.2 h |
| Red | 24.2–47.7 h | 23.5 h |
| No added dye (shown in gray in Figure A-24 and Figure A-26) | 47.7–64.1 h | 16.4 h |

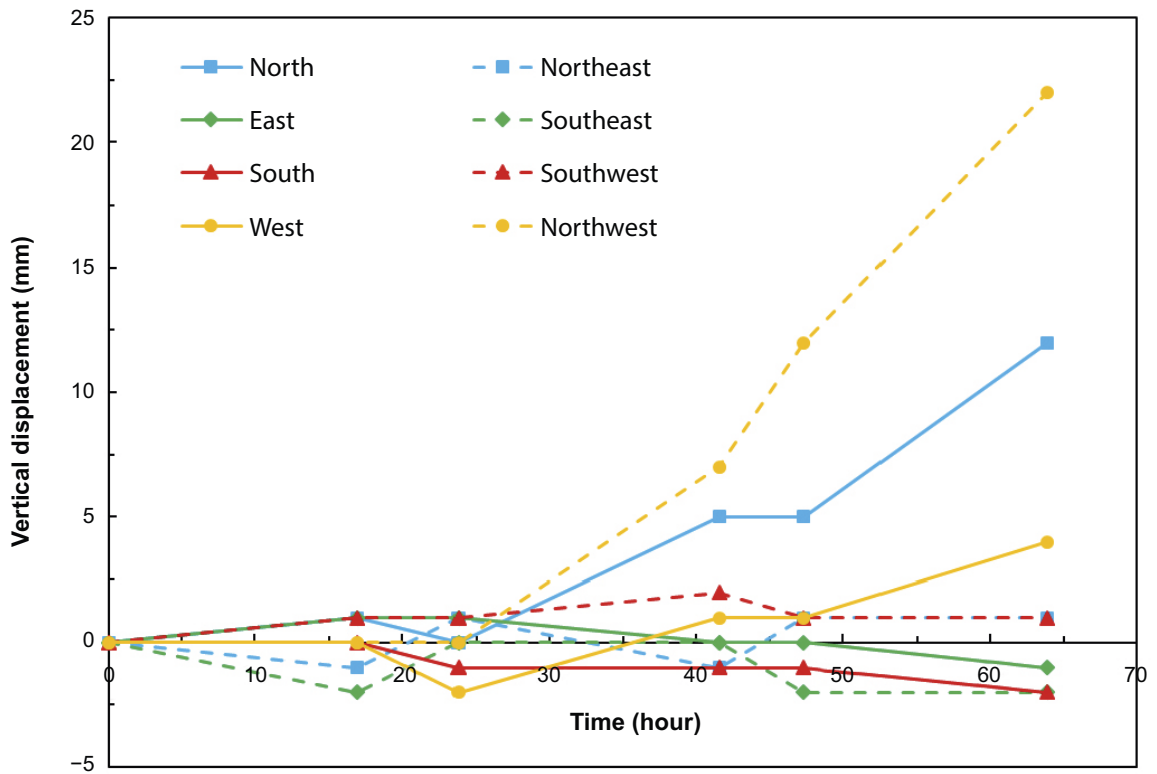


Figure A-22. Vertical displacement of the pellet filling as a function of time over the course of test 07.

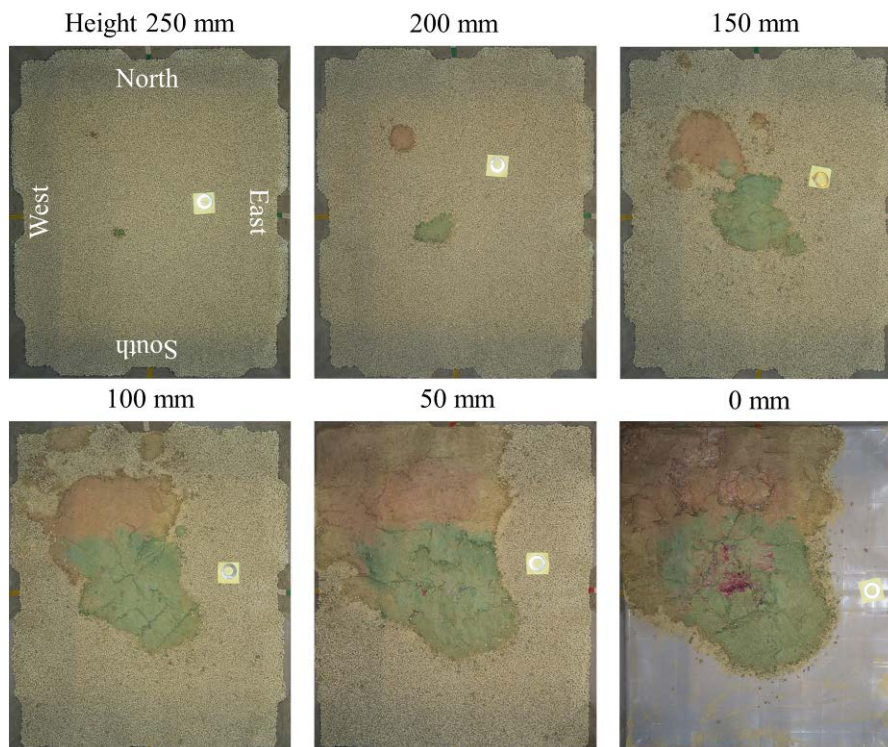


Figure A-23. Appearance of test 07 during dismantling over the height of the pellet filling at the end of the test (after 64.1 hours). Note, the inlet point located in the middle of the bottom of the box.

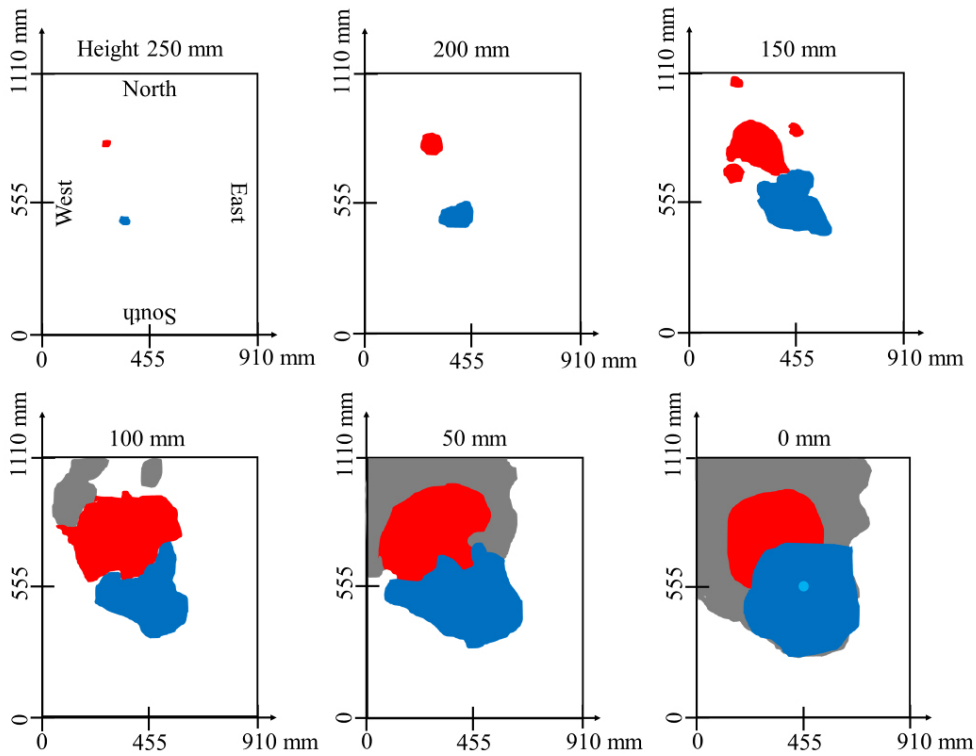


Figure A-24. Qualitative wetting pattern threshold (colors correspond to the dyes over the specific time spans according to Table 4-4 and white areas to visually dry pellet zones) images for test 07 over the pellet filling zones at the end of the test (after 64.1 hours). The inlet point was located in the middle of the bottom of the box (marked with light blue dot).

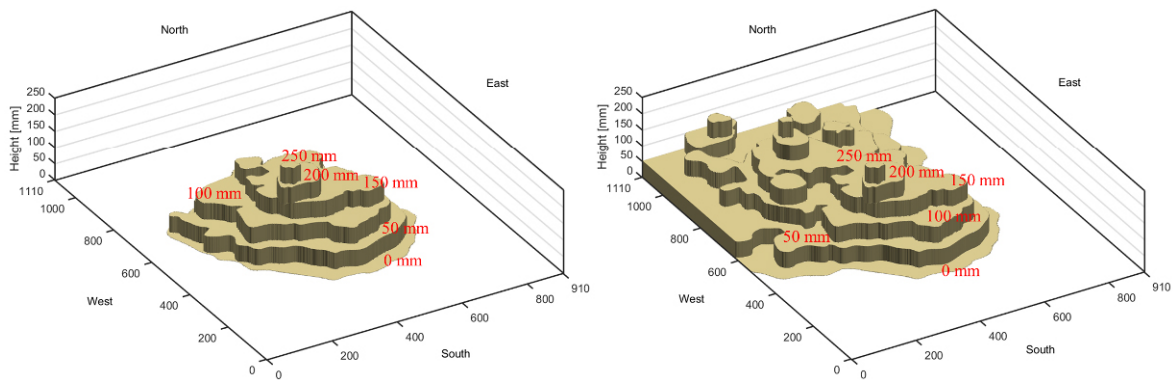


Figure A-25. 3D qualitative wetting pattern images for test 07 over the pellet filling volume after 24.2 hours (left) and at the end of the test (right). The height of surface layers in 3D wetting pattern image is indicated with red color. Note, sharp edges between layers are artefacts due to 3D image was constructed from 2D images (see Martikainen et al. 2017) by image analysis program.

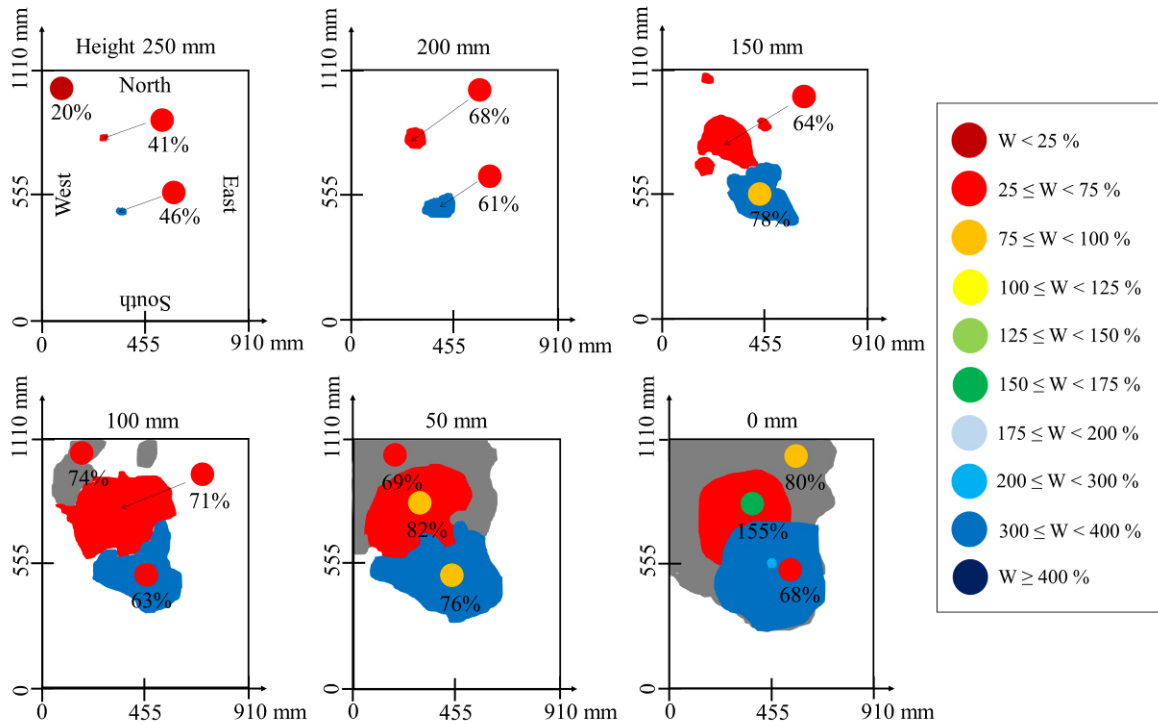


Figure A-26. Water content distributions over the height of the pellet-filled volume at the end of test 07 (64.1 hours) in 2D (top) and 3D images (bottom). Circles indicate the sampling location at each height and water content value is indicated with colors (see table in the bottom image). Black and gray outline represents wetting pattern at each height in bottom image. Note, the inlet point was located in the bottom of the box (marked with light blue dot in bottom image).

SKB is responsible for managing spent nuclear fuel and radioactive waste produced by the Swedish nuclear power plants such that man and the environment are protected in the near and distant future.

skb.se